Size effects in martensitic microstructures: finite-strain phase field model versus sharp-interface approach[☆]

K. Tůma[a], S. Stupkiewicz[a,*], H. Petryk[a]

[a]*Institute of Fundamental Technological Research (IPPT), Polish Academy of Sciences, Pawińskiego 5B, 02-106 Warsaw, Poland.*

Abstract

A finite-strain phase field model for martensitic phase transformation and twinning in shape memory alloys is developed and confronted with the corresponding sharp-interface approach extended to interfacial energy effects. The model is set in the energy framework so that the kinetic equations and conditions of mechanical equilibrium are fully defined by specifying the free energy and dissipation potentials. The free energy density involves the bulk and interfacial energy contributions, the latter describing the energy of diffuse interfaces in a manner typical for phase-field approaches. To ensure volume preservation during martensite reorientation at finite deformation within a diffuse interface, it is proposed to apply linear mixing of the logarithmic transformation strains. The physically different nature of phase interfaces and twin boundaries in the martensitic phase is reflected by introducing two order-parameters in a hierarchical manner, one as the reference volume fraction of austenite, and thus of the whole martensite, and the second as the volume fraction of one variant of martensite in the martensitic phase only. The microstructure evolution problem is given a variational formulation in terms of incremental fields of displacement and order parameters, with unilateral constraints on volume fractions explicitly enforced by applying the augmented Lagrangian method. As an application, size-dependent microstructures with diffuse interfaces are calculated for the cubic-to-orthorhombic transformation in a CuAlNi shape memory alloy and compared with the sharp-interface microstructures with interfacial energy effects.

Keywords: phase-field method, microstructure, martensite, size effects, shape memory alloys

1. Introduction

Martensitic phase transformation plays an essential role in many material systems. Shape memory alloys (SMA) represent a well-known example of the class of materials in which the martensitic transformation is crucial for their unusual and spectacular behaviour associated with shape recovery, pseudoelasticity, and related effects (Otsuka and Wayman, 1998; Bhattacharya, 2003).

The martensitic transformation frequently proceeds by formation and evolution of complex microstructures involving several martensite variants. Commonly observed martensitic microstructures can be predicted by the classical crystallographic theory of martensite (Ball and James, 1987), which is essentially based on the thermodynamic argument of free energy minimization. In practice, the use of the crystallographic theory reduces to purely geometric relationships expressing compatibility of stress-free phases, as in the earlier theory of Wechsler et al. (1953). Those compatibility conditions imply that the interfaces, such as sharp twin interfaces and microstructured austenite–twinned martensite interfaces, are planar. Laminated microstructures are thus energetically prefer-

able and are indeed commonly observed at various scales, while more complex microstructures, e.g., wedges, necessarily combine planar interfaces (Otsuka and Wayman, 1998; Bhattacharya, 2003).

It is well known that minimization of the bulk free energy alone leads to infinitely fine microstructures, which is not acceptable for both physical and theoretical reasons. The energy of interfaces, if accounted for in the energy minimization, can provide a natural intrinsic length scale and thus govern size effects and set characteristic dimensions of microstructure (Khachaturyan, 1983; Ball and James, 1987; Roytburd, 1998; Aubry et al., 2003; Petryk et al., 2006, 2010). It has been recently shown by Petryk and Stupkiewicz (2012) that infinitely fine evolving laminates, as a rule, exhibit intrinsic instability, while evolving laminates of finite spacing are stabilized by the interfacial energy.

While sharp-interface models are useful in the analysis of basic microstructures, without or with size effects as in the references above, the modelling of migration of sharp interfaces becomes more difficult in the cases of evolution of complex microstructures whose pattern is unknown in advance. Then the attractive alternative is to use the phase-field approach where diffuse phase interfaces are characterized by order parameters that are continuous in space and time and replace a discontinuous phase change at sharp interfaces. In this paper the point of view is adopted that 'the diffuseness of the phase field exists on a scale that is below the microstructure scale of interest' (Steinbach, 2009). The interface thickness scale is set by a numerical parameter (ℓ) that need not be related to characteristic dimensions of real microstructures. Basic features of the phase-field method and references to numerous earlier papers with a variety of specific applications can be found in recent articles (Chen, 2002; Moelans et al., 2008; Steinbach, 2009; Wang and Li, 2010; Mamivand et al., 2013; Levitas, 2014). An important advantage of the phase-field approach is that tracking of individual interfaces is avoided, and efficient computational schemes can be developed in which the formation and evolution of microstructure can be modeled on a fixed computational mesh or grid.

In this paper, the phase-field method is used to study the first-order phase transition between austenite and twinned martensite in the *finite-deformation* framework. In the small-strain setting, similar problems have been examined in many papers, e.g., (Wang and Khachaturyan, 1997; Jin et al., 2001; Levitas and Preston, 2002; Ahluvalia et al., 2004; Lei et al., 2010), while finite-strain phase-field models are restricted to few formulations dealing with multivariant transformation (Levitas et al., 2009; Levin et al., 2013) or only with twinning (Clayton and Knap, 2011; Hildebrand and Miehe, 2012). A non-trivial step is to define the elastic finite-strain bulk energy in the diffuse interface domain where distinct phases or martensite variants coexist in the model at each material point, cf. (Mosler et al., 2014). This can be done by defining a mixing rule for finite transformation strains. In the case of a mixture of two twin-related martensite variants, the mixing rule can be formulated using the twinning equation, i.e. by exploiting compatibility of the two variants (Clayton and Knap, 2011; Hildebrand and Miehe, 2012). This approach has its advantages, however, it is not directly generalizable to cases other than twinning. In a general approach, which does not require compatibility of the phases at zero stress, the transformation strain of the phase mixture can be defined as the average of the individual transformation strains, typically weighted by non-linear functions of order parameters (Levitas et al., 2009; Levin et al., 2013). A problem in the approaches based on mixing of the common finite strain measures (as the Green strain or stretch tensor) is that changes in the volume, none for twinning and small for phase transition in SMA, are not treated consistently. To remove this drawback, in this paper we propose a direct superposition of *logarithmic* transformation strains multiplied by volume fractions of the respective phases within diffuse interfaces, followed by an exponential map to obtain the transformation stretch tensor for the mixture. In this way, volume is preserved exactly during martensite reorientation within diffuse interfaces.

The major aim of this paper is twofold: (i) to develop a multi-phase field model for the mixture of austenite and twinned martensite at finite deformation, and (ii) to examine consistency of the finite-strain phase-field modelling of size-dependent microstructures in SMA with the sharp-interface energy approach. The model (i) introduces certain novel ingredients to be discussed in more detail later on, and the topic (ii) appears to be addressed for the first time.

In the model, two order-parameters are introduced to adequately describe the involved three constituents: the austenite and two variants of martensite. One of the distinctive features of the present finite-strain model is that it uses the order-parameters treated in a *hierarchical* manner, as at small strain in (Shu and Yen, 2008; Lei et al., 2010), which differs from the conventional phase field models. The first order-parameter is the reference volume fraction of austenite (and thus specifies the *total* volume fraction of martensite as well), and the second one is the *relative* volume fraction of one variant of martensite in the martensitic phase only, both taken in a stress-free reference configuration of austenite as the parent phase. As a result, two types of interfaces (austenite–martensite and martensite–martensite) are described in a natural manner. The bulk free energy and the dissipation potential are formulated accordingly. The model is set in the energy-rate minimization framework so that the equilibrium and kinetic equations are fully defined by specifying the free energy function and the dissipation potential. Computational treatment is based on implicit time integration of the rate-problem and spatial discretization by the finite element method. One of the novel features of the present phase-field model is that the physical constraints on the volume fractions are explicitly enforced by applying the augmented Lagrangian method.

As an application, microstructures with twin interfaces and austenite–twinned martensite interfaces in a CuAlNi shape memory alloy undergoing cubic-to-orthorhombic transformation are studied. Anisotropy of elastic response of each phase is included, taking the material parameters for this alloy from the materials science literature (Suezawa and Sumino, 1976; Yasunaga et al., 1983). Several realistic microstructures are computed by solving a generalized 2D boundary value problem in a plane orthogonal to both the twinning and habit planes. This special class of 2D problems has been examined earlier using the sharp-interface approach (Maciejewski et al., 2005; Stupkiewicz et al., 2007, 2012), while related phase-field computations have only been found in (Lei et al., 2010), at small strain and without studying size effects.

The paper is organized as follows. In the next section, the basic concepts of phase-field modelling of twinning at finite deformation are recalled, with the novel aspects such as the logarithmic mixing rule and the variational formulation including bound constraints on the order parameter. In Section 3, the model is extended to austenite and two variants of martensite by introducing hierarchical order-parameters and the corresponding free energy and dissipation potentials. A non-trivial transition from the variational rate formulation to the incremental one is also discussed. The finite-element implementation, including the augmented Lagrangian treatment of inequality constraints, is described in Section 4, followed by several numerical examples presented in Section 5. A class of generalized plane strain problems is defined, which is then used to study martensite–martensite and austenite–twinned martensite microstructures in CuAlNi alloy. The related size effects predicted by the phase-field model are compared to the analytical estimates derived in Appendix B by using the sharp-interface energy approach.

2. Finite-strain phase-field model of twinning

2.1. Phase-field evolution equation

In the phase-field approach, a twin boundary is approximated by a continuous transition of the order parameter between two states corresponding to the individual martensite variants. The order parameter η is taken here equal to the volume fraction of a crystallographic variant I of martensite, characterized by the (Bain) transformation stretch tensor $\mathbf{U}_I$. Throughout Section 2 austenite is assumed absent, nevertheless, both η and $\mathbf{U}_I$ are defined in a fixed stress-free reference configuration of *austenite* as the parent phase. Under the physical constraint $0 \leq \eta \leq 1$, the second twin-related martensite variant J characterized by transformation stretch $\mathbf{U}_J$ has the reference volume fraction equal to $(1 - \eta)$. The volume fraction η is taken here as a non-conserved order parameter in the framework of the classical phase-field approach. Accordingly, the basic Ginzburg–Landau equation for the material time derivative $\dot{\eta} = \mathrm{d}\eta/\mathrm{d}t$ of the order parameter η is adopted, cf. e.g., (Penrose and Fife, 1990; Chen, 2002),

$$\dot{\eta} = -L \frac{\delta \mathcal{F}}{\delta \eta}, \tag{1}$$

where $L > 0$ is a mobility parameter. $\mathcal{F}$ is the Helmholtz free energy functional over a body domain $B \subset \mathbb{R}^3$ in a fixed reference configuration,

$$\mathcal{F}[\mathbf{u}, \eta] = \int_B F(\nabla \mathbf{u}, \eta, \nabla \eta) \, \mathrm{d}\mathbf{X}, \tag{2}$$

of density F dependent smoothly on $\nabla \mathbf{u}$ and on both η and its gradient $\nabla \eta$. Disregarding for simplicity a possible dependence of F on the reference position vector $\mathbf{X}$, the gradient ∇ is defined here in the stress-free reference configuration of homogeneous austenite. The right-hand expression in Eq. (1) is the classical functional derivative defined by

$$\frac{\delta \mathcal{F}}{\delta \eta} = \frac{\partial F}{\partial \eta} - \nabla \cdot \frac{\partial F}{\partial \nabla \eta}. \tag{3}$$

In order to account for the physical constraint $0 \leq \eta \leq 1$, the evolution equation (1) is rewritten as

$$\dot{\eta} = \begin{cases} 0 & \text{if } \eta = 0 \text{ and } \dfrac{\delta \mathcal{F}}{\delta \eta} \geq 0, \\[2mm] 0 & \text{if } \eta = 1 \text{ and } \dfrac{\delta \mathcal{F}}{\delta \eta} \leq 0, \\[2mm] -L \dfrac{\delta \mathcal{F}}{\delta \eta} & \text{otherwise.} \end{cases} \tag{4}$$

The free energy density F is split into the bulk (F_B) and interfacial (F_Γ) parts, viz.

$$F(\nabla \mathbf{u}, \eta, \nabla \eta) = F_\mathrm{B}(\nabla \mathbf{u}, \eta) + F_\Gamma(\eta, \nabla \eta), \tag{5}$$

where $\mathbf{u}$ denotes a differentiable displacement vector field. The interfacial free energy density is taken in a typical form

$$F_\Gamma(\eta, \nabla \eta) = \gamma_\mathrm{tw} \left(\frac{3\ell}{2} |\nabla \eta|^2 + \frac{6}{\ell} \eta^2 (1 - \eta)^2 \right), \tag{6}$$

where ℓ defines the length-scale across the interface. The form (6) is composed of the squared gradient of η and the standard double-well potential in η. The scaling factors in the formula (6) for F_Γ are chosen such that in the direction normal to the interface there is

$$\inf_{\substack{\eta \in \mathcal{W} \\ \eta(-\infty)=0, \eta(+\infty)=1}} \int_{-\infty}^{+\infty} \left(\frac{3\ell}{2} \left| \frac{\mathrm{d}\eta}{\mathrm{d}X} \right|^2 + \frac{6}{\ell} \eta^2 (1 - \eta)^2 \right) \mathrm{d}X = 1, \tag{7}$$

so that γ_tw represents the equilibrium twin-interface energy density per unit reference area (cf. Clayton and Knap, 2011; Hildebrand and Miehe, 2012), for simplicity taken as an orientation-independent constant. Clearly, the functional space $\mathcal{W}$ must be suitably chosen so that the integral in Eq. (7) makes sense. In this case, it is apparent that $\mathcal{W}$ can be the space of real functions which are square-integrable together with their gradient (i.e. $W^{1,2}(\mathbb{R})$). Henceforward, specification of a suitable functional space will be omitted, except the essential constraints which will be specified explicitly.

2.2. Bulk free energy

The deformation gradient $\mathbf{F} = \mathbf{I} + \nabla \mathbf{u}$, where $\mathbf{I}$ is the second-order identity tensor, is split into the elastic part $\mathbf{F}_\mathrm{e}$ and transformational part by the standard multiplicative decomposition $\mathbf{F} = \mathbf{F}_\mathrm{e} \mathbf{F}_\mathrm{t}$, such that $\mathbf{F}_\mathrm{t}$ defines a *local* unstressed configuration (called intermediate configuration).

In this section where only twinning is considered, the bulk free energy F_B is reduced to the strain energy density of anisotropic elasticity, adopted for simplicity (in the SMA context following

Kružík et al. (2005); Maciejewski et al. (2005)) as a quadratic function of the elastic Green strain $\mathbf{E}_e = \frac{1}{2}(\mathbf{F}_e^T \mathbf{F}_e - \mathbf{I})$, viz.

$$F_B(\nabla \mathbf{u}, \eta) = \frac{1}{2} (\det \mathbf{F}_t(\eta)) \, \mathbf{E}_e(\nabla \mathbf{u}, \eta) \cdot \mathbf{L}(\eta) \, \mathbf{E}_e(\nabla \mathbf{u}, \eta) \, , \tag{8}$$

where $\mathbf{L}(\eta)$ is the elastic stiffness tensor. Here, F_B is the density taken per unit volume of the *parent* phase (austenite). In view of typically small elastic strains, the assumption of the elastic strain energy density as a quadratic function of the specific elastic strain is physically not restrictive.

Within a diffuse interface, the tensors $\mathbf{L}$ and $\mathbf{F}_t$ corresponding to a local mixture are to be defined. In view of the atomic-size thickness of real twin interfaces, the actual mechanical properties of the interface layer are expected to be influenced by factors on a scale below the range of validity of the continuum models, and are thus unlikely to be fully determinable by continuum homogenization alone. Therefore, it seems reasonable to use simple definitions, as those adopted below, to enable possibly clear understanding of the approximations involved.

The classical Voigt rule, of the well-known interpretation, is adopted here for determining the average anisotropic elastic stiffness moduli tensor,

$$\mathbf{L}(\eta) = \eta \mathbf{L}_I + (1 - \eta) \mathbf{L}_J \, , \tag{9}$$

where $\mathbf{L}_I$ is the elastic stiffness tensor of the variant I evaluated in the intermediate configuration characterized by $\mathbf{U}_I$.

It remains to define $\mathbf{F}_t$ as a function of the order parameter η for a mixture of two selected variants of martensite corresponding to the Bain stretch tensors $\mathbf{U}_I$ and $\mathbf{U}_J$. However, straightforward averaging of the transformation stretch or Green strain tensors violates the required preservation of volume during twinning. Therefore, we propose a new mixing rule applied to *logarithmic* transformation strains,

$$\mathbf{U}_t(\eta) = \exp\left(\eta \log \mathbf{U}_I + (1 - \eta) \log \mathbf{U}_J\right) \, , \tag{10}$$

followed by an exponential map to obtain the transformation stretch tensor for the mixture. Using expression (10), the transformational part $\mathbf{F}_t(\eta)$ of the total deformation gradient $\mathbf{F}$ is defined as a pure stretch, thus $\mathbf{F}_t(\eta) = \mathbf{U}_t(\eta)$. The rotation is a part of the solution and it is included in $\mathbf{F}_e$, which is consistent with the absence of rotations associated with $\mathbf{U}_I$ and $\mathbf{U}_J$ in the assumed formulae (9) and (10).

It is easily proven by using Jacobi's formula that

$$\det \mathbf{U}_t(\eta) = \det\left(\exp\left(\eta \log \mathbf{U}_I + (1-\eta)\log \mathbf{U}_J\right)\right) = \exp\left(\eta \operatorname{tr}\left(\log \mathbf{U}_I\right) + (1-\eta)\operatorname{tr}\left(\log \mathbf{U}_J\right)\right)$$
$$= \exp\left(\eta \log\left(\det \mathbf{U}_I\right) + (1-\eta)\log\left(\det \mathbf{U}_J\right)\right) = (\det \mathbf{U}_I)^\eta (\det \mathbf{U}_J)^{(1-\eta)} . \tag{11}$$

As the volume is preserved during twinning, i.e. $\det \mathbf{U}_I = \det \mathbf{U}_J$, it follows that $\det \mathbf{U}_t(\eta) = \det \mathbf{U}_I = \det \mathbf{U}_J$, so that the mixing rule (10) preserves the volume for arbitrary η, which is not the case for linear mixing of strain measures other than the logarithmic one, see the numerical illustration in Section 3.1. In the computer implementation of the mixing rule (10), the matrix exponential and its derivatives are efficiently computed using the closed-form representation developed by Korelc and Stupkiewicz (2014).

A different volume-preserving mixing rule has been used in (Clayton and Knap, 2011; Hildebrand and Miehe, 2012), which directly exploits the rank-one connection that results from the twinning equation (54), see Section 5.1. However, that approach is only applicable for two twin-related variants and cannot be generalized to more variants or phases. The present mixing rule (10) is more general, see Section 3.1.

2.3. Global variational formulation of the rate-problem

In this section, the governing rate-equations are formulated in a weak form as a global variational principle convenient for further numerical implementation.

First, by adding to the free energy $\mathcal{F}$ a potential energy Ω of external loads, assumed conservative, the global potential energy functional of the fields of displacement and order parameter, $(\mathbf{u}, \eta)$, and their gradients as functions of $\mathbf{X}$ over B, is

$$\mathcal{E}[\mathbf{u}, \eta] = \mathcal{F}[\mathbf{u}, \eta] + \Omega[\mathbf{u}], \tag{12}$$

The fields of $(\mathbf{u}, \eta)$ vary in time t and are subjected in general to time-dependent boundary conditions, while time t is usually omitted as a parameter to simplify the notation. The evolution problem is considered to be quasi-static, i.e. the inertia effects are neglected. The condition of mechanical equilibrium at each instant is expressed in a standard way as stationarity of functional $\mathcal{E}$ with respect to arbitrary kinematically admissible variations $\delta\mathbf{u}$, viz.

$$\delta_{\mathbf{u}}\mathcal{E}[\mathbf{u}, \eta] = 0 \qquad \forall \delta\mathbf{u} \text{ such that } \mathbf{u}, \mathbf{u} + \delta\mathbf{u} \in \mathcal{V}_{\mathbf{u}} = \{\mathbf{u} \in \mathcal{V} \mid \mathbf{u} = \bar{\mathbf{u}}(t) \text{ on } \partial B_u\}, \tag{13}$$

where ∂B_u is the closed part of the boundary of B on which the time-dependent displacement boundary condition $\mathbf{u} = \bar{\mathbf{u}}(t)$ is prescribed. $\mathcal{V}$ is a suitable space of three-dimensional vector functions over B that are extendable to the closure of B such that all the boundary conditions imposed over ∂B make a mathematical sense.

In the particular case when Ω corresponds to the nominal surface traction prescribed over $\partial B_T = \partial B \setminus \partial B_u$, so that

$$\Omega[\mathbf{u}] = -\int_{\partial B_T} \mathbf{T}(t) \cdot \mathbf{u} \, \mathrm{d}S, \tag{14}$$

the equilibrium condition (13) reduces to the local conditions of linear momentum balance

$$\frac{\delta\mathcal{F}}{\delta\mathbf{u}} = \mathbf{0} \quad \text{in } B \qquad \text{and} \qquad \frac{\partial F}{\partial\nabla\mathbf{u}} \cdot \mathbf{n} = \mathbf{T} \quad \text{on } \partial B_T, \tag{15}$$

where $\mathbf{n}$ is an outward unit normal to ∂B. In the absence of body forces, $\delta\mathcal{F}/\delta\mathbf{u} = -\nabla \cdot \mathbf{S}^{\mathrm{T}}$, where $\mathbf{S} = \partial F/\partial\nabla\mathbf{u}$ is the first Piola–Kirchhoff stress tensor.

An equivalent formulation of mechanical equilibrium is obtained by considering the rate functional $\dot{\mathcal{E}} = \mathrm{d}\mathcal{E}/\mathrm{d}t$ and by requiring stationarity of $\dot{\mathcal{E}}$ with respect to arbitrary kinematically admissible variations $\delta\dot{\mathbf{u}}$ of velocities,

$$\delta_{\dot{\mathbf{u}}}\dot{\mathcal{E}}[\dot{\mathbf{u}}, \dot{\eta}; \mathbf{u}, \eta] = 0 \qquad \forall \delta\dot{\mathbf{u}} \text{ such that } \dot{\mathbf{u}}, \dot{\mathbf{u}} + \delta\dot{\mathbf{u}} \in \mathcal{V}_{\dot{\mathbf{u}}} = \{\dot{\mathbf{u}} \in \mathcal{V} \mid \dot{\mathbf{u}} = \dot{\bar{\mathbf{u}}} \text{ on } \partial B_u\}. \tag{16}$$

Note that $\dot{\mathcal{E}}$ is a linear functional of $(\dot{\mathbf{u}}, \dot{\eta})$, hence $\delta_{\dot{\mathbf{u}}}\dot{\mathcal{E}}[\dot{\mathbf{u}}, \dot{\eta}; \mathbf{u}, \eta]$ does not depend on $\dot{\mathbf{u}}$. The variational equality (16) imposes in effect the equilibrium condition on the displacement field $\mathbf{u}$, which is evident from Eq. (13), rather than on the velocity field $\dot{\mathbf{u}}$, which might be conjectured from Eq. (16) alone.

In order to obtain a variational formulation of the evolution problem including the evolution equation (1), the standard quadratic dissipation potential

$$\mathcal{D}[\dot{\eta}] = \int_B D(\dot{\eta}) \, \mathrm{d}\mathbf{X}, \qquad D(\dot{\eta}) = \frac{1}{2L}\dot{\eta}^2 \tag{17}$$

is assumed. Clearly, the local dissipation rate is $\frac{\mathrm{d}D}{\mathrm{d}\dot{\eta}}\dot{\eta}$. For simplicity, we assume that η satisfies the zero Neumann boundary condition over the whole boundary ∂B, so that

$$\frac{\partial F}{\partial\nabla\eta} \cdot \mathbf{n} = 0 \quad \text{over } \partial B, \tag{18}$$

while, if needed, a corresponding Dirichlet boundary condition could be introduced on a part of the boundary ∂B in a standard way.

Finally, the following global rate-potential Π is introduced in a given state $(\mathbf{u}, \eta)$, similarly as in (Hildebrand and Miehe, 2012),

$$\Pi[\dot{\mathbf{u}}, \dot{\eta}; \mathbf{u}, \eta] = \dot{\mathcal{E}}[\dot{\mathbf{u}}, \dot{\eta}; \mathbf{u}, \eta] + \mathcal{D}[\dot{\eta}]. \tag{19}$$

It can be easily verified that fulfillment of the unconstrained evolution equation (1) is equivalent to stationarity of the functional $\Pi[\dot{\mathbf{u}}, \dot{\eta}; \mathbf{u}, \eta]$ with respect to $\dot{\eta}$. Furthermore, since $\Pi[\dot{\mathbf{u}}, \dot{\eta}; \mathbf{u}, \eta]$ is quadratic in $\dot{\eta}$, stationarity of $\Pi[\dot{\mathbf{u}}, \dot{\eta}; \mathbf{u}, \eta]$ implies its minimum with respect to $\dot{\eta}$. The constrained evolution equation (4) can thus be equivalently formulated as a constrained minimization of $\Pi[\dot{\mathbf{u}}, \dot{\eta}; \mathbf{u}, \eta]$ at $\dot{\mathbf{u}} \equiv \mathbf{0}$. At the same time, the fulfillment of the equilibrium condition (16) is equivalent to the existence of a trivial minimum (constancy) of the linear functional $\Pi[\dot{\mathbf{u}}, \dot{\eta}; \mathbf{u}, \eta] = \dot{\mathcal{E}}[\dot{\mathbf{u}}, \dot{\eta}; \mathbf{u}, \eta]$ at $\dot{\eta} \equiv 0$.

In conclusion, the complete quasi-static evolution problem defined by equations (4) and (13), starting from a given initial state at some instant t_0, is reduced to the constrained minimization problem

$$\forall t > t_0 \text{ find } \min_{\dot{\mathbf{u}} \in \mathcal{V}_{\dot{\mathbf{u}}}, \dot{\eta} \in \mathcal{W}_{\dot{\eta}}} \Pi[\dot{\mathbf{u}}, \dot{\eta}; \mathbf{u}, \eta] \text{ subject to } \dot{\eta} \geq 0 \text{ if } \eta = 0 \text{ and } \dot{\eta} \leq 0 \text{ if } \eta = 1, \qquad (20)$$

where $\mathcal{W}_{\dot{\eta}}$ is a suitable space. Recall that $\dot{\mathbf{u}} \in \mathcal{V}_{\dot{\mathbf{u}}}$ satisfies the boundary condition $\dot{\mathbf{u}} = \dot{\bar{\mathbf{u}}}$ on ∂B_u.

The general variational structure of the present finite-strain phase-field model of twinning is similar to that of Hildebrand and Miehe (2012). The difference is that the physical bounds on the order parameter η are here imposed explicitly, which influences the computational algorithm.

The present model is summarized in a concise form in Box 1.

(i) Multiplicative decomposition of deformation gradient and the logarithmic mixing rule

$$\mathbf{F} = \mathbf{F}_{\mathrm{e}}\mathbf{F}_{\mathrm{t}}, \qquad \mathbf{F}_{\mathrm{t}} = \mathbf{U}_{\mathrm{t}} = \exp\left(\eta \log \mathbf{U}_I + (1 - \eta)\log \mathbf{U}_J\right)$$

(ii) Bulk free energy density

$$F_{\mathrm{B}} = \frac{1}{2}(\det \mathbf{F}_{\mathrm{t}})\mathbf{E}_{\mathrm{e}} \cdot \mathbf{L}\mathbf{E}_{\mathrm{e}}, \qquad \mathbf{L} = \eta \mathbf{L}_I + (1 - \eta)\mathbf{L}_J, \qquad \mathbf{E}_{\mathrm{e}} = \frac{1}{2}(\mathbf{F}_{\mathrm{e}}^{\mathrm{T}}\mathbf{F}_{\mathrm{e}} - \mathbf{I})$$

(iii) Interfacial energy density

$$F_{\Gamma} = \gamma_{\mathrm{tw}}\left(\frac{3\ell}{2}|\nabla\eta|^2 + \frac{6}{\ell}\eta^2(1 - \eta)^2\right)$$

(iv) Total free energy density, dissipation potential and global rate-potential

$$F = F_{\mathrm{B}} + F_{\Gamma}, \qquad D = \frac{1}{2L}\dot{\eta}^2, \qquad \Pi = \int_B \left(\dot{F} + D\right) \mathrm{d}\mathbf{X} + \dot{\Omega}$$

(v) Global variational principle (constrained minimization problem)

$$\forall t > t_0 \text{ find } \min_{\dot{\mathbf{u}}, \dot{\eta}} \Pi[\dot{\mathbf{u}}, \dot{\eta}; \mathbf{u}, \eta] \text{ subject to } 0 \leq \eta \leq 1$$

Box 1: Summary of the finite-strain phase-field model of twinning.

Remark 1. The minimum principle (20) with respect to $\dot{\eta}$ can be interpreted as a version of the classical Onsager–Ziegler thermodynamic extremal principle, cf. Fischer et al. (2014) for a recent overview, extended to unilateral constraints. As explained above, minimization (20) with respect to $\dot{\mathbf{u}}$ is equivalent to the global condition of mechanical equilibrium that is imposed on the current displacement field $\mathbf{u}$, and not on velocity field $\dot{\mathbf{u}}$. Equations (1) and (15) are just the Euler–Lagrange equations corresponding to the variational problem (20).

Remark 2. Parameters L and ℓ set characteristic scales of time and length, respectively. They are treated here as numerical regularization parameters.

Remark 3. The twinning equation of the crystallographic theory of martensite (based on transformation strain compatibility across twin interfaces at zero stress) is not used in the present phase-field model of twinning. However, it is expected and confirmed by the numerical results presented in the later sections that the orientation of diffuse twin interfaces agrees with that predicted by the twinning equation.

2.4. Implicit time integration scheme

The rate-problem discussed above will be now discretized in time. To this end, we consider a typical time step such that $t_{n+1} = t_n + \tau$, where $\tau > 0$ is the time increment. The solution at t_n is known from the previous time step, and the respective fields are denoted by $(\mathbf{u}_n, \eta_n)$. The subscript $n + 1$ corresponding to the time instant t_{n+1} is omitted below to make the notation more compact, so that at t_{n+1} the unknown fields of displacement and order parameter are denoted by $(\mathbf{u}, \eta)$ and their rates by $(\dot{\mathbf{u}}, \dot{\eta})$, thus

$$(\mathbf{u}_{n+1}, \eta_{n+1}, \dot{\mathbf{u}}_{n+1}, \dot{\eta}_{n+1}) \to (\mathbf{u}, \eta, \dot{\mathbf{u}}, \dot{\eta}).$$

In the incremental setting, the minimization problem (20) is solved at the end of the time step, i.e. at t_{n+1}, which corresponds to the implicit backward-Euler time integration scheme applied to the rate problem. Since $\dot{\mathcal{E}}$ depends linearly on $(\dot{\mathbf{u}}, \dot{\eta})$, the rate-potential at t_{n+1} is approximated as

$$\Pi[\dot{\mathbf{u}}, \dot{\eta}; \mathbf{u}, \eta] = \dot{\mathcal{E}}[\dot{\mathbf{u}}, \dot{\eta}; \mathbf{u}, \eta] + \mathcal{D}[\dot{\eta}] \approx \frac{1}{\tau} \left(\mathcal{E}[\mathbf{u}, \eta] - \mathcal{E}[\mathbf{u}_n, \eta_n] \right) + \mathcal{D}\left[(\eta - \eta_n)/\tau \right], \qquad (21)$$

and it is apparent that it now depends on the unknowns $(\mathbf{u}, \eta)$. Accordingly, minimization is performed with respect to $(\mathbf{u}, \eta)$, and this is conveniently formulated by minimization of the incremental potential Π_τ,

$$\text{find} \min_{\mathbf{u} \in \mathcal{V}_\mathbf{u}, \eta \in \mathcal{W}_\eta} \Pi_\tau[\mathbf{u}, \eta] \text{ subject to } 0 \leq \eta \leq 1, \qquad (22)$$

where the space $\mathcal{V}_\mathbf{u}$ of displacements fields is as in Eq. (13), and $\mathcal{W}_\eta$ is a suitable space of order parameters. The incremental potential Π_τ is defined as follows

$$\Pi_\tau[\mathbf{u}, \eta] = \mathcal{E}[\mathbf{u}, \eta] + \tau \mathcal{D}\left[(\eta - \eta_n)/\tau \right], \qquad (23)$$

and η_n is known hence the dependence of Π_τ on η_n is not indicated.

Assuming that Ω, the potential energy of external loads, is given by Eq. (14), the explicit form of the incremental potential Π_τ is

$$\Pi_\tau[\mathbf{u}, \eta] = \int_B \left(F(\nabla\mathbf{u}, \eta, \nabla\eta) + D_\tau(\eta) \right) \mathrm{d}\mathbf{X} - \int_{\partial B_T} \mathbf{T} \cdot \mathbf{u} \, \mathrm{d}S, \qquad (24)$$

where the incremental dissipation potential D_τ is defined as

$$D_\tau(\eta) = \tau D\left(\frac{\eta - \eta_n}{\tau} \right) = \frac{\tau}{2L} \left(\frac{\eta - \eta_n}{\tau} \right)^2. \qquad (25)$$

Finally, in order to arrive at the incremental evolution equations in explicit form, we introduce the Lagrange functional $\mathcal{L}$,

$$\mathcal{L}[\mathbf{u}, \eta, \lambda^-, \lambda^+] = \Pi_\tau[\mathbf{u}, \eta] - \int_B \left(\eta \lambda^- + (1 - \eta)\lambda^+ \right) \mathrm{d}\mathbf{X}, \qquad (26)$$

where λ^- and λ^+ are the fields of Lagrange multipliers that enforce the constraints $\eta \geq 0$ and $1 - \eta \geq 0$, respectively. The necessary condition for the constrained minimum of Π_τ is expressed in a standard way as stationarity of $\mathcal{L}$ with respect to $(\mathbf{u}, \eta)$,

$$0 = \delta_{(\mathbf{u}, \eta)} \mathcal{L}[\mathbf{u}, \eta, \lambda^-, \lambda^+] \qquad \forall (\delta\mathbf{u}, \delta\eta) \in \mathcal{V}_\mathbf{u}^0 \times \mathcal{W}_\eta, \quad \mathcal{V}_\mathbf{u}^0 = \{\mathbf{u} \in \mathcal{V} \mid \mathbf{u} = \mathbf{0} \text{ on } \partial B_u\}, \qquad (27)$$

along with the usual Kuhn–Tucker conditions

$$\eta \geq 0, \quad \lambda^- \geq 0, \quad \eta\lambda^- = 0 \qquad \text{and} \qquad 1 - \eta \geq 0, \quad \lambda^+ \geq 0, \quad (1 - \eta)\lambda^+ = 0, \qquad (28)$$

where

$$\delta_{(\mathbf{u},\eta)}\mathcal{L}[\mathbf{u}, \eta, \lambda^-, \lambda^+] = \int_B \left(\frac{\partial F}{\partial \nabla \mathbf{u}} \cdot \nabla \delta \mathbf{u} + \left(\frac{\partial F}{\partial \eta} + \frac{\partial D_\tau}{\partial \eta} - \lambda^- + \lambda^+ \right) \delta \eta + \frac{\partial F}{\partial \nabla \eta} \cdot \nabla \delta \eta \right) \mathrm{d}\mathbf{X}$$
$$- \int_{\partial B_T} \mathbf{T} \cdot \delta \mathbf{u} \, \mathrm{d}S. \quad (29)$$

In the computational scheme developed in this work, the inequality constraints are efficiently treated using the augmented Lagrangian method, as described in Section 4.1.

3. Phase-field model for austenite and two variants of martensite

This section is an extension of the preceding section and is based on similar concepts. Therefore, only the most essential changes are commented in the succeeding text in more detail, and formulae adapted straightforwardly are just given as sufficiently obvious in the light of explanations provided earlier.

3.1. Bulk free energy

The total deformation gradient $\mathbf{F}$ at a material point representing a phase mixture is split into the elastic part $\mathbf{F}_e$ and average transformational part $\mathbf{F}_t$, i.e. $\mathbf{F} = \mathbf{F}_e\mathbf{F}_t$. Suppose that the material consists of austenite and N different variants of martensite, of the volume fractions ν_0 and ν_i, respectively, all in the stress-free reference configuration of austenite, with the physical constraint $\sum_{i=0}^{N} \nu_i = 1$. In analogy to Section 2, the transformational part $\mathbf{F}_t$ is defined by linear mixing of the *logarithmic* transformation strains of the phases (variants),

$$\mathbf{F}_t = \mathbf{U}_t = \exp\left(\sum_{i=0}^{N} \nu_i \log \mathbf{U}_i \right), \qquad (30)$$

and anisotropic elastic stiffness matrix for the mixture is constructed by the Voigt rule,

$$\mathbf{L} = \sum_{i=0}^{N} \nu_i \mathbf{L}_i. \qquad (31)$$

The bulk free energy density is assumed in the form

$$F_B = \sum_{i=0}^{N} \nu_i F_i^0 + \frac{1}{2}(\det \mathbf{F}_t)\mathbf{E}_e \cdot \mathbf{L}\mathbf{E}_e, \qquad (32)$$

where F_i^0 are the chemical free energies corresponding to the i-th phase. Taking unstressed austenite as a reference, we have for austenite $F_a^0 = F_0^0 = 0$ and for martensite variants $F_m^0 = F_1^0 = F_2^0$.

The model is now specified for three phases/variants ($N = 2$), i.e. austenite and two variants of martensite. The physically different nature of austenite–martensite interfaces and twin boundaries in the martensitic phase is reflected by introducing two order parameters $(\eta_0, \eta_1 \equiv \eta)$ in a *hierarchical* manner, such that

$$\nu_0 = \eta_0, \qquad \nu_1 = (1 - \eta_0)\,\eta, \qquad \nu_2 = (1 - \eta_0)\,(1 - \eta), \qquad (33)$$

9

where η_0 is the volume fraction of austenite, η the *relative* volume fraction of the first variant (I) of martensite and $(1 - \eta)$ the *relative* volume fraction of the second variant (J) of martensite. Accordingly, on account of $\log \mathbf{U}_0 = \mathbf{0}$ for austenite, we obtain

$$\mathbf{U}_t(\eta, \eta_0) = \exp\left((1 - \eta_0)\left(\eta \log \mathbf{U}_I + (1 - \eta) \log \mathbf{U}_J\right)\right), \tag{34}$$

$$\mathbf{L}(\eta, \eta_0) = \eta_0 \mathbf{L}_a + (1 - \eta_0)\left(\eta \mathbf{L}_I + (1 - \eta)\mathbf{L}_J\right). \tag{35}$$

As discussed in Section 2.2, the mixing rule (34) preserves the volume under variations of η alone, i.e. $\det \mathbf{F}_t = const$ at fixed η_0 for all $\eta \in [0, 1]$, see Fig. 1(b). In contrast, for linear mixing of transformation stretches according to $\mathbf{F}_t^* = \mathbf{U}_t^* = \eta_0 \mathbf{I} + (1 - \eta_0)(\eta \mathbf{U}_I + (1 - \eta)\mathbf{U}_J)$, the volume changes are not treated consistently, as depicted in Fig. 1(a).
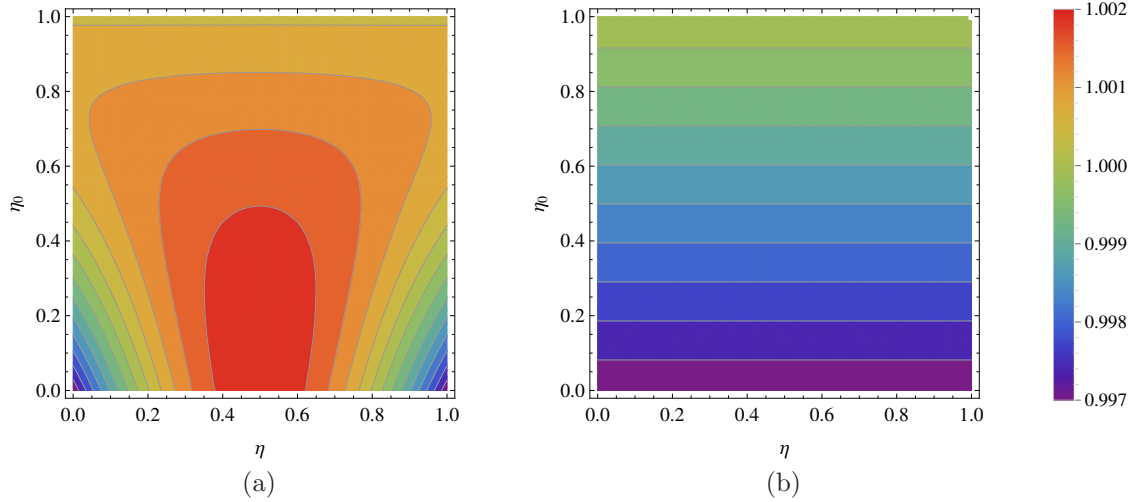

Figure 1: Dependence of $\det \mathbf{F}_t$ on η and η_0 for (a) linear and (b) logarithmic mixing of transformation stretches (computed for CuAlNi alloy, see Section 5).

3.2. Interfacial energy

The total interfacial energy density $F_\Gamma = F_\Gamma^{am} + F_\Gamma^{mm}$ consists of the interfacial energy between austenite and some variant of martensite F_Γ^{am}, in analogy to Eq. (6) taken as

$$F_\Gamma^{am}(\eta_0, \nabla\eta_0) = \gamma_{am}\left(\frac{3\ell}{2}|\nabla\eta_0|^2 + \frac{6}{\ell}\eta_0^2(1 - \eta_0)^2\right), \tag{36}$$

and the interfacial energy between two martensite variants F_Γ^{mm}. A natural option for the second energy, with the same length scale ℓ across austenite–martensite and martensite–martensite interfaces, would be

$$\tilde{F}_\Gamma^{mm}(\eta, \eta_0, \nabla\eta) = (1 - \eta_0)\gamma_{tw}\left(\frac{3\ell}{2}|\nabla\eta|^2 + \frac{6}{\ell}\eta^2(1 - \eta)^2\right), \tag{37}$$

where the interfacial energy density γ_{tw} is scaled by $(1 - \eta_0)$. However, in this case there would be no equation for η when $\eta_0 = 1$. While it is physically justified, it is not acceptable in numerical calculations, because the resulting problem is ill-posed. Accordingly, instead of $\tilde{F}_\Gamma^{mm}$, we assume a modified interfacial energy form

$$F_\Gamma^{mm}(\eta, \eta_0, \nabla\eta) = \gamma_{tw}\left(\frac{3\ell}{2}|\nabla\eta|^2 + (1 - \eta_0)\frac{6}{\ell}\eta^2(1 - \eta)^2\right), \tag{38}$$

10

which, from a mathematical point of view, substituted in the global variational formulation given below will provide the Laplace equation for η when $\eta_0 = 1$. The above formula can be interpreted as scaling the interfacial energy density γ_{tw} in formula (6) by $\sqrt{1 - \eta_0}$ (thus neglecting it for η_0 going to one) with simultaneous scaling of the characteristic length ℓ by $1/\sqrt{1 - \eta_0}$. Obviously, in each case the formula (6) is recovered in a martensite domain where $\eta_0 = 0$.

3.3. Dissipation potential

Similarly as in Section 2, a quadratic dissipation potential is assumed it terms of the rates of order parameters. The dissipation rate associated with martensite variant reorientation is taken quadratic in $\dot{\eta}$ and proportional to the volume fraction $(1 - \eta_0)$ of martensite. In turn, the dissipation rate due to phase transformation between austenite and martensite is taken quadratic in $\dot{\eta}_0$ and independent of the martensite composition, i.e. independent of η. Under these assumptions, the quadratic rate-dependent, local dissipation potential takes the form

$$D(\dot{\eta}, \dot{\eta}_0, \eta_0) = \frac{1}{2L_0}\dot{\eta}_0^2 + \frac{1}{2L}(1 - \eta_0)\dot{\eta}^2. \tag{39}$$

where L and L_0 denote the respective mobility parameters. Note that, in accord with the hierarchical structure of the order parameters, their influence on dissipation is not symmetric. The dissipation potential as a function of $(\dot{\eta}_0, \dot{\eta})$ is now *state-dependent* through the current value of volume fraction η_0 of austenite, being still independent of η. If $\eta_0 \to 1$ then the martensite disappears, so that $\dot{\eta}$ looses its physical meaning and, consequently, ceases to affect the dissipation potential in Eq. (39).

3.4. Global variational formulation of the rate-problem

The formula (19) for the global rate-potential remains valid with the exception that the order parameter η_0 is now an additional state-variable and its rate $\dot{\eta}_0$ is an additional unknown function, assumed to satisfy the boundary condition analogous to condition (18). Otherwise, the phase-field problem formulation is fully analogous to Eq. (20): minimization of the potential Π with respect to the admissible rate-fields $(\dot{\mathbf{u}}, \dot{\eta}, \dot{\eta}_0)$ from appropriate spaces (omitted here), i.e.

$$\forall t > t_0 \text{ find } \min_{\dot{\mathbf{u}}, \dot{\eta}, \dot{\eta}_0} \Pi[\dot{\mathbf{u}}, \dot{\eta}, \dot{\eta}_0; \mathbf{u}, \eta, \eta_0] \text{ subject to } 0 \leq \eta, \eta_0 \leq 1, \tag{40}$$

where $\dot{\mathbf{u}}$ satisfies the boundary condition $\dot{\mathbf{u}} = \dot{\bar{\mathbf{u}}}$ on ∂B_u. The bound constraints on η and η_0 in the minimization problem (40) imply that $\dot{\eta} \geq 0$ or ≤ 0 if $\eta = 0$ or 1, respectively, and similar conditions hold for $\dot{\eta}_0$.

The proposed model is summarized in a concise form in Box 2. For completeness, the basic field equations satisfied by a solution to the variational rate-problem (40) are provided in Appendix A.

3.5. Implicit time integration scheme

Until now the formulation of the problem followed that of Section 2. The main difference between the two models, apart from the additional order parameter, is that the dissipation potential (39) is state-dependent, i.e. it depends on η_0 in addition to the rates $\dot{\eta}$ and $\dot{\eta}_0$, while the dissipation potential (17) depends only on the rate $\dot{\eta}$. As a result, the variational structure of the time-discrete problem will be different. In particular, the incremental problem derived below by using the implicit (backward Euler) time integration scheme will not take the form of a genuine minimization problem.

The rate-potential Π at t_{n+1} is now approximated as

$$\hat{\Pi}[\dot{\mathbf{u}}, \dot{\eta}, \dot{\eta}_0; \mathbf{u}, \eta, \eta_0; \hat{\eta}_0] = \dot{\mathcal{E}}[\dot{\mathbf{u}}, \dot{\eta}, \dot{\eta}_0; \mathbf{u}, \eta, \eta_0] + \mathcal{D}[\dot{\eta}, \dot{\eta}_0; \hat{\eta}_0] \approx$$
$$\frac{1}{\tau}\left(\mathcal{E}[\mathbf{u}, \eta, \eta_0] - \mathcal{E}[\mathbf{u}_n, \eta_n, \eta_{0,n}]\right) + \mathcal{D}\left[(\eta - \eta_n)/\tau, (\eta_0 - \eta_{0,n})/\tau; \hat{\eta}_0\right], \quad (41)$$

where an additional variable $\hat{\eta}_0$ has been introduced to reflect the state-dependence of the dissipation potential (39). This quantity coincides with η_0, however, for consistency with the underlying rate

11

(i) Multiplicative decomposition of deformation gradient and the logarithmic mixing rule

$$\mathbf{F} = \mathbf{F}_{\mathrm{e}}\mathbf{F}_{\mathrm{t}}, \qquad \mathbf{F}_{\mathrm{t}} = \mathbf{U}_{\mathrm{t}} = \exp\left((1-\eta_0)\left(\eta\log\mathbf{U}_I + (1-\eta)\log\mathbf{U}_J\right)\right)$$

(ii) Bulk free energy density

$$F_{\mathrm{B}} = (1-\eta_0)F_{\mathrm{m}}^0 + \frac{1}{2}(\det\mathbf{F}_{\mathrm{t}})\mathbf{E}_{\mathrm{e}}\cdot\mathbf{L}\mathbf{E}_{\mathrm{e}}, \qquad \mathbf{L} = \eta_0\mathbf{L}_{\mathrm{a}} + (1-\eta_0)\left(\eta\mathbf{L}_I + (1-\eta)\mathbf{L}_J\right)$$

(iii) Interfacial energy density

$$F_{\Gamma} = \gamma_{\mathrm{am}}\left(\frac{3\ell}{2}|\nabla\eta_0|^2 + \frac{6}{\ell}\eta_0^2(1-\eta_0)^2\right) + \gamma_{\mathrm{tw}}\left(\frac{3\ell}{2}|\nabla\eta|^2 + (1-\eta_0)\frac{6}{\ell}\eta^2(1-\eta)^2\right)$$

(iv) Total free energy density, dissipation potential and global rate-potential

$$F = F_{\mathrm{B}} + F_{\Gamma}, \qquad D = \frac{1}{2L_0}\dot{\eta}_0^2 + \frac{1}{2L}(1-\eta_0)\dot{\eta}^2, \qquad \Pi = \int_B\left(\dot{F} + D\right)\mathrm{d}\mathbf{X} + \dot{\Omega}$$

(v) Global variational principle (constrained minimization problem)

$$\forall t > t_0 \text{ find } \min_{\dot{\mathbf{u}},\dot{\eta},\dot{\eta}_0} \Pi[\dot{\mathbf{u}},\dot{\eta},\dot{\eta}_0;\mathbf{u},\eta,\eta_0] \text{ subject to } 0 \le \eta, \eta_0 \le 1$$

Box 2: Summary of the phase-field model for austenite and two variants of martensite.

principle (40) at t_{n+1} the substitution $\hat{\eta}_0 = \eta_0$ is to be made *after* evaluation of the derivative of the above right-hand side expression with respect to η_0. The additional variable $\hat{\eta}_0$ is consequently introduced also in the incremental potential Π_τ defined by

$$\Pi_\tau[\mathbf{u},\eta,\eta_0;\hat{\eta}_0] = \mathcal{E}[\mathbf{u},\eta,\eta_0] + \tau\mathcal{D}\left[(\eta-\eta_n)/\tau,(\eta_0-\eta_{0,n})/\tau;\hat{\eta}_0\right], \tag{42}$$

which otherwise is a generalization of the incremental potential defined by Eq. (23). The explicit form of Π_τ in case of external potential (14) is thus the following:

$$\Pi_\tau[\mathbf{u},\eta,\eta_0;\hat{\eta}_0] = \int_B\left(F(\nabla\mathbf{u},\eta,\eta_0,\nabla\eta,\nabla\eta_0) + D_\tau(\eta,\eta_0,\hat{\eta}_0)\right)\mathrm{d}\mathbf{X} - \int_{\partial B_T}\mathbf{T}\cdot\mathbf{u}\,\mathrm{d}S, \tag{43}$$

where the local incremental dissipation potential D_τ takes the form

$$D_\tau(\eta,\eta_0,\hat{\eta}_0) = \tau D\left(\frac{\eta-\eta_n}{\tau},\frac{\eta_0-\eta_{0,n}}{\tau},\hat{\eta}_0\right) = \frac{\tau}{2L_0}\left(\frac{\eta_0-\eta_{0,n}}{\tau}\right)^2 + \frac{\tau}{2L}(1-\hat{\eta}_0)\left(\frac{\eta-\eta_n}{\tau}\right)^2. \tag{44}$$

Minimization in the rate-problem (40) is performed with respect to the rates at fixed state. Accordingly, upon time integration, the minimization should be performed with respect to η and η_0, but not with respect to $\hat{\eta}_0$. Since $\hat{\eta}_0 = \eta_0$ depends on an unknown solution of the minimization problem, the complete problem at hand cannot be formulated as a genuine minimization problem. Rather, the incremental problem is formulated as follows

$$\text{find } \min_{\mathbf{u}\in\mathcal{V}_{\mathbf{u}},\eta,\eta_0\in\mathcal{W}_\eta} \Pi_\tau[\mathbf{u},\eta,\eta_0;\hat{\eta}_0]\big|_{\hat{\eta}_0=\eta_0} \text{ subject to } 0 \le \eta,\eta_0 \le 1. \tag{45}$$

Similar incomplete minimization problems occur, for example, in the different context of frictional contact problems (Alart and Curnier, 1991).

Remark 4. The form (45) of the incremental problem shows that a given extremum principle formulated in terms of the rates need not lead straightforwardly to an analogous variational principle

for small but finite increments. The state-dependence of the rate potential, if present, requires a separate treatment.

A variational form accounting for the constrains on the order parameters can be obtained by introducing the Lagrange functional $\mathcal{L}$,

$$\mathcal{L}[\mathbf{u}, \eta, \eta_0, \lambda^-, \lambda^+, \lambda_0^-, \lambda_0^+; \hat{\eta}_0] = \Pi_\tau[\mathbf{u}, \eta, \eta_0; \hat{\eta}_0] - \int_B \left(\eta\lambda^- + (1-\eta)\lambda^+ + \eta_0\lambda_0^- + (1-\eta_0)\lambda_0^+ \right) \mathrm{d}\mathbf{X}, \quad (46)$$

with $\lambda^\pm$ and $\lambda_0^\pm$ the Lagrange multipliers corresponding to η and η_0, respectively, and by requiring stationarity of $\mathcal{L}$ with respect to $(\mathbf{u}, \eta, \eta_0)$ at fixed $\hat{\eta}_0 = \eta_0$, namely

$$0 = \delta_{(\mathbf{u}, \eta, \eta_0)} \mathcal{L}[\mathbf{u}, \eta, \eta_0, \lambda^-, \lambda^+, \lambda_0^-, \lambda_0^+; \hat{\eta}_0]\big|_{\hat{\eta}_0 = \eta_0} \qquad \forall (\delta\mathbf{u}, \delta\eta, \delta\eta_0) \in \mathcal{V}_\mathbf{u}^0 \times \mathcal{W}_\eta \times \mathcal{W}_\eta, \qquad (47)$$

along with the Kuhn-Tucker conditions

$$\eta \geq 0, \quad \lambda^- \geq 0, \quad \eta\lambda^- = 0 \qquad \text{and} \qquad 1 - \eta \geq 0, \quad \lambda^+ \geq 0, \quad (1-\eta)\lambda^+ = 0, \qquad (48\text{a})$$

$$\eta_0 \geq 0, \quad \lambda_0^- \geq 0, \quad \eta_0\lambda_0^- = 0 \qquad \text{and} \qquad 1 - \eta_0 \geq 0, \quad \lambda_0^+ \geq 0, \quad (1-\eta_0)\lambda_0^+ = 0, \qquad (48\text{b})$$

where

$$\delta_{(\mathbf{u}, \eta, \eta_0)} \mathcal{L}[\mathbf{u}, \eta, \eta_0, \lambda^-, \lambda^+, \lambda_0^-, \lambda_0^+; \hat{\eta}_0]\big|_{\hat{\eta}_0 = \eta_0} = \int_B \frac{\partial F}{\partial \nabla \mathbf{u}} \cdot \nabla \delta\mathbf{u} \, \mathrm{d}\mathbf{X} - \int_{\partial B_T} \mathbf{T} \cdot \delta\mathbf{u} \, \mathrm{d}S$$

$$+ \int_B \left(\left(\frac{\partial F}{\partial \eta} + \frac{\partial D_\tau}{\partial \eta}\bigg|_{\hat{\eta}_0 = \eta_0} - \lambda^- + \lambda^+ \right) \delta\eta + \frac{\partial F}{\partial \nabla\eta} \cdot \nabla\delta\eta \right) \mathrm{d}\mathbf{X}$$

$$+ \int_B \left(\left(\frac{\partial F}{\partial \eta_0} + \frac{\partial D_\tau}{\partial \eta_0}\bigg|_{\hat{\eta}_0 = \eta_0} - \lambda_0^- + \lambda_0^+ \right) \delta\eta_0 + \frac{\partial F}{\partial \nabla\eta_0} \cdot \nabla\delta\eta_0 \right) \mathrm{d}\mathbf{X}. \quad (49)$$

As already mentioned, in the computational scheme used in this work, the inequality constraints are efficiently treated using the augmented Lagrangian method, see Section 4.1.

4. Finite element implementation

4.1. Augmented Lagrangian method

The augmented Lagrangian method has been used in this work in order to conveniently enforce the inequality constraints $0 \leq \eta \leq 1$ and $0 \leq \eta_0 \leq 1$; see Bertsekas (1996) for a general description of the augmented Lagrangian method and Stupkiewicz and Petryk (2013) for its application to the bound constraints imposed on the volume fraction of martensite in SMA. The method is briefly described below, more details concerning the augmented Lagrangian treatment of bound constraints in SMA can be found in Stupkiewicz and Petryk (2013).

Consider first the incremental phase-field model of twinning discussed in Section 2.4 and governed by the constrained minimization problem (22),

$$\text{find} \quad \min_{\mathbf{u} \in \mathcal{V}_\mathbf{u}, \eta \in \mathcal{W}_\eta} \Pi_\tau[\mathbf{u}, \eta] \quad \text{subject to} \quad 0 \leq \eta \leq 1. \qquad (50)$$

In the augmented Lagrangian method, this problem is transformed into a *smooth and unconstrained* saddle-point problem,

$$\text{find} \quad \min_{\mathbf{u} \in \mathcal{V}_\mathbf{u}, \eta \in \mathcal{W}_\eta} \max_{\lambda \in \mathcal{W}_\lambda} \mathcal{L}_{\mathrm{AL}}[\mathbf{u}, \eta, \lambda], \qquad (51)$$

for the Lagrange functional $\mathcal{L}_{\mathrm{AL}}$,

$$\mathcal{L}_{\mathrm{AL}}[\mathbf{u}, \eta, \lambda] = \Pi_\tau[\mathbf{u}, \eta] + \int_B L_{\mathrm{AL}}(\eta, \lambda) \, \mathrm{d}\mathbf{X}. \qquad (52)$$

13

Here, λ denotes the field of Lagrange multipliers (from a suitable space $\mathcal{W}_\lambda$) associated with the inequality constraints in (50), and function $L_{\mathrm{AL}}(\eta, \lambda)$ is a continuously differentiable function defined as follows:

$$L_{\mathrm{AL}}(\eta, \lambda) = \begin{cases} \lambda(\eta - \eta^-) + \dfrac{\varrho}{2}(\eta - \eta^-)^2 & \text{if } \lambda + \varrho\eta < \varrho\eta^-, \\[2mm] -\dfrac{1}{2\varrho}\lambda^2 & \text{if } \varrho\eta^- \leq \lambda + \varrho\eta \leq \varrho\eta^+, \\[2mm] \lambda(\eta - \eta^+) + \dfrac{\varrho}{2}(\eta - \eta^+)^2 & \text{if } \varrho\eta^+ < \lambda + \varrho\eta, \end{cases} \tag{53}$$

where $\eta^- = 0$, $\eta^+ = 1$ and $\varrho > 0$ is a regularization parameter. Note that the two inequality constraints in the bound constraint $0 \leq \eta \leq 1$ are now enforced using a *single* Lagrange multiplier λ.

The necessary condition for the minimum of the original problem is expressed as stationarity of the Lagrange functional $\mathcal{L}_{\mathrm{AL}}$. Stationarity of $\mathcal{L}_{\mathrm{AL}}$ with respect to $\mathbf{u}$ yields the mechanical equilibrium in weak form, while stationarity with respect to η yields the incremental evolution equation for η. This is similar to the usual Lagrange multiplier technique, as used in Section 3.5. However, the beneficial feature of the augmented Lagrangian method is that stationarity of the Lagrangian $\mathcal{L}_{\mathrm{AL}}$ with respect to both η and λ ensures also fulfillment of the Kuhn–Tucker conditions (48), with $\lambda = -\lambda^-$ for $\eta = 0$ and $\lambda = \lambda^+$ for $\eta = 1$, which can be verified directly.

Remark 5. The augmented Lagrangian method applied to an inequality-constrained problem leads thus to exact fulfillment of the Kuhn–Tucker conditions at the saddle point of $\mathcal{L}_{\mathrm{AL}}$, without any need to increase a regularization parameter unboundedly.

This feature of the augmented Lagrangian method provides the basis for developing efficient computational schemes for inequality-constrained problems. Since the Lagrangian is continuously differentiable, the nonlinear algebraic equations obtained after finite-element discretization can be solved using the (semi-smooth) Newton method simultaneously for the primal variables and Lagrange multipliers.

Considering now the more general model introduced in Section 3, we recall that the dissipation potential (39) corresponding to the hierarchical phase-field model for austenite and two variants of martensite is state-dependent, as discussed in Section 3.5. As a result, the corresponding incremental problem (45) is not a genuine minimization problem. Nevertheless, the augmented Lagrangian method can be applied by combining the incremental formulation derived in Section 3.5 with the approach presented above. Specifically, the bound constraints on η and η_0 are enforced exactly as described above, and stationarity of the resulting Lagrangian at fixed $\hat\eta_0 = \eta_0$ yields the incremental equations. The details are omitted here.

4.2. Discretization and Newton-based solution

The numerical examples reported in this paper are restricted to generalized plane strain problems in which all three components of the displacement field are considered but dependent on two spatial variables so that the problem is computationally two-dimensional, see Section 5.1 below. The unknowns are displacements, order parameters and the Lagrange multipliers enforcing the bound constraints on the order parameters. For periodic unit cell computations, additional Lagrange multipliers are used to enforce periodicity.

The present computer implementation has been performed using the *AceGen/AceFEM* system (Korelc, 2002, 2009). *AceGen* is an automatic code generation system while *AceFEM* is a finite element environment closely integrated with *AceGen*. The automatic differentiation (AD) technique is implemented in *AceGen* which permits an efficient and robust implementation. Specifically, referring to the augmented Lagrangian formulation outlined in Section 4.1, the implementation amounts to adequate coding of the scalar Lagrangian $\mathcal{L}_{\mathrm{AL}}$. The element quantities such as the residual vector, which is a derivative of the Lagrangian with respect to the nodal quantities, and the tangent matrix, which is a derivative of the residual vector, are then obtained by applying the AD technique. A detailed description of this approach can be found in (Korelc, 2009).

The finite element discretization is rather standard, hence only the most important features are briefly commented below. The two-dimensional domain B is approximated by B^h with a polygonal boundary, and B^h is discretized by regular quadrilaterals. All unknowns are approximated by piecewise-bilinear continuous elements. Numerical integration is used at the element level: Π_τ is integrated with the Gaussian quadrature and the Lagrange functions with the nodal quadrature.

In the present implementation, the transformation part $\mathbf{F}_t$ of the deformation gradient is assumed constant within the element with the value evaluated at the element center. The piecewise-bilinear approximation of the order parameters implies a continuous, approximately piecewise-bilinear approximation of $\mathbf{F}_t$. At the same time, the deformation gradient $\mathbf{F}$ is a gradient of a piecewise-bilinear displacement field, and, in particular, it is not continuous. Mutually inconsistent approximation of $\mathbf{F}$ and $\mathbf{F}_t$ induces spurious stresses within diffuse interfaces, and this undesirable effect is avoided by adopting element-wise constant $\mathbf{F}_t$.

It is recalled here that $\mathbf{F}_t$ is defined by the logarithmic mixing rule, see Eqs. (10) and (34). The implementation involves thus computation of the matrix exponential as well as its first and second derivatives, the later needed for the tangent matrix. In general, the implementation of the matrix exponential and, in particular, of its derivatives is not straightforward, and it is usually associated with a significant computational cost. In this work, the matrix exponential is efficiently implemented using the closed-form representation recently developed by Korelc and Stupkiewicz (2014).

The nonlinear equations resulting from the finite-element discretization are solved using the (semi-smooth) Newton method. Here, a fully-coupled monolithic finite-element approach is adopted that treats all the unknowns simultaneously. Application of the AD technique leads to exact linearization of the finite-element equations, i.e. an exact tangent matrix is obtained. This is crucial for achieving quadratic convergence of the Newton method and for overall efficiency of the computational scheme. A direct linear solver has been used in the present computations.

Physical processes corresponding to phase transition and microstructure evolution can involve both slow and rapid changes. To efficiently handle such processes, we use a heuristic adaptive time stepping scheme where the time step is automatically adjusted such that the number of Newton iterations be between six and eight.

In order to obtain a non-uniform solution when starting from a uniform initial configuration, a stochastic perturbation term (Langevin noise) is frequently added to the right-hand side of the evolution equation (1), cf. (Wang and Khachaturyan, 1997; Artemev et al., 2000). In this work, spatially random imperfections of the mobility parameters L and L_0, typically by 1%, are introduced for that purpose. A higher imperfection of 5% was needed to trigger microstructure formation in Section 5.4. While this numerical approach lacks a physical background, its benefit is that a steady-state solution is not affected by the introduced imperfection.

5. Numerical examples

The major aim of the numerical examples reported in this work is to study the austenite–twinned martensite microstructures and the related size effects, with CuAlNi alloy taken as an example, by the phase-field method in direct comparison with the sharp-interface approach. Both approaches include interfacial energy effects, although in a different manner and under different assumptions. It is of special interest to compare phase-field predictions with analytic estimates available from the sharp-interface approach for laminate microstructures described by the crystallographic theory of martensite.

Below, basic equations of the classical crystallographic theory of martensite are briefly recalled, and a special two-dimensional problem for a three-dimensional microstructure is formulated for microstructure parameters predicted by that theory. Next, microstructures involving two martensite variants are studied followed by microstructures involving austenite and two variants of martensite.

5.1. Basic equations of the crystallographic theory of martensite

In the vast majority of SMA, a single variant of martensite cannot form a compatible interface with austenite in stress-free conditions. However, such an interface can be formed between austenite and twinned martensite. The corresponding microstructure is predicted by the classical crystallographic theory of martensite (Wechsler et al., 1953; Ball and James, 1987; Bhattacharya, 2003) by using the twinning equation,

$$\mathbf{R}\mathbf{U}_I - \mathbf{U}_J = \mathbf{a} \otimes \mathbf{l}, \tag{54}$$

and the habit plane equation,

$$\hat{\mathbf{R}}\left(\hat{\eta}\mathbf{R}\mathbf{U}_I + (1-\hat{\eta})\mathbf{U}_J\right) - \mathbf{I} = \mathbf{b} \otimes \mathbf{m}, \tag{55}$$

which express the kinematic compatibility between undeformed austenite and the mixture of unstressed (but rotated) martensite variants I and J with transformation stretches $\mathbf{U}_I$ and $\mathbf{U}_J$, respectively. The unknowns in Eqs. (54) and (55) are the twinning plane normal $\mathbf{l}$, the habit plane normal $\mathbf{m}$, vectors $\mathbf{a}$ and $\mathbf{b}$, rotations $\mathbf{R}$ and $\hat{\mathbf{R}}$, and the twin fraction $\hat{\eta}$.

The habit plane equation (55) describes the macroscopic compatibility of the austenite and a fine laminate of two twin-related variants. According to the crystallographic theory, the deformation gradients of the first martensitic variant $\mathbf{F}_I$, the other martensitic variant $\mathbf{F}_J$ and austenite $\mathbf{F}_a$ are equal to:

$$\mathbf{F}_I = \hat{\mathbf{R}}\mathbf{R}\mathbf{U}_I, \quad \mathbf{F}_J = \hat{\mathbf{R}}\mathbf{U}_J, \quad \mathbf{F}_a = \mathbf{I}, \tag{56}$$

and all correspond to the stress-free conditions and thus to minimal (zero) elastic strain energy. In an actual microstructure with a finite twin spacing, the stresses do vanish far from the interface; however, a transition layer with nonzero micro-stresses must develop along the interface, since local incompatibility is accommodated by elastic strains. The corresponding interfacial energy of elastic micro-strains and the morphology of the transition layer have been studied using the sharp-interface approach in (Maciejewski et al., 2005; Stupkiewicz et al., 2007, 2012). In those works, the analysis has been carried out for the microstructures being essentially two-dimensional so that the displacements, strains and stresses do not depend on the coordinate orthogonal to $\mathbf{l}$ and $\mathbf{m}$. Accordingly, the corresponding elasticity problem has been formulated as a generalized plane strain problem in a plane parallel to both $\mathbf{l}$ and $\mathbf{m}$; however, with three nonzero components of the displacement field.

5.2. Generalized plane strain problem

An analogous assumption is adopted in the present work in the context of diffuse-interface phase-field modelling. Specifically, a two-dimensional generalized plane strain problem is considered, and the analysis is carried out in a plane parallel to $\mathbf{l}$ and $\mathbf{m}$ in the reference configuration of stress-free austenite. While this assumption introduces a constraint on the class of microstructures that can develop, the corresponding reduction of the spatial dimension of the problem allows us to simulate the problem with a high resolution (i.e. for a fine mesh and/or large computational domain) that would not be reachable at present in case of general, fully three-dimensional problems.

In all examples reported below, the microstructure is controlled by prescribing the average deformation gradient $\langle \mathbf{F} \rangle$ to be equal to $\bar{\mathbf{F}}$, thus

$$\langle \mathbf{F} \rangle = \bar{\mathbf{F}}, \qquad \langle \cdot \rangle = \frac{1}{|B|}\int_B (\cdot)\,\mathrm{d}\mathbf{X}, \tag{57}$$

where $\bar{\mathbf{F}}$ is constructed by weighting the deformation gradients resulting from the crystallographic theory, Eq. (56), according to

$$\bar{\mathbf{F}} = \bar{\eta}_0\mathbf{F}_a + (1-\bar{\eta}_0)\left(\bar{\eta}\mathbf{F}_I + (1-\bar{\eta})\mathbf{F}_J\right), \tag{58}$$

where $\bar{\eta}$ and $\bar{\eta}_0$ are control parameters that are expected to be correlated with the averaged values of the order parameters η and η_0, respectively. The condition $\langle \mathbf{F} \rangle = \bar{\mathbf{F}}$ is enforced either by prescribing the Dirichlet boundary condition on the whole boundary of the domain B,

$$\mathbf{u}(\mathbf{X}) = \bar{\mathbf{u}}(\mathbf{X}) \quad \text{for } \mathbf{X} \in \partial B, \quad \text{where } \bar{\mathbf{u}} = (\bar{\mathbf{F}} - \mathbf{I})\mathbf{X}, \tag{59}$$

or by enforcing periodic boundary conditions

$$\mathbf{u}(\mathbf{X}) = (\bar{\mathbf{F}} - \mathbf{I})\mathbf{X} + \tilde{\mathbf{u}}(\mathbf{X}) \quad \text{for } \mathbf{X} \in \partial B, \quad \text{where } \tilde{\mathbf{u}} \text{ is } B\text{-periodic.} \tag{60}$$

The later situation corresponds to the analysis of a periodic unit cell, and in that case also the order parameters (η_0, η) are assumed to be periodic.

By adopting the boundary conditions specified above, the idea here is to determine the general features of the microstructure along with transition layers and related size effects in a manner that enables direct comparison with the features of laminated microstructures determined by the sharp-interface approach with interfacial energy effects summarized in Appendix B.

For consistency in visualization of results for problems involving both austenite and martensite (Sections 5.6 and 5.7), the same orientation of vectors $\mathbf{m}$ and $\mathbf{l}$ is adopted also for problems involving two variants of martensite only, i.e. for $\bar{\eta}_0 = 0$ (Sections 5.4 and 5.5), with $\mathbf{l}$ chosen horizontal in the figures.

For problems involving two variants of martensite only, the total volume of the domain B does not depend on $\bar{\eta}$ by construction, i.e. $\det \bar{\mathbf{F}} = \det \mathbf{U}_I = \det \mathbf{U}_J$. At the same time, the logarithmic mixing rule (10) guarantees that the transformation part of the deformation gradient is locally isochoric. Accordingly, volume changes are treated consistently and no spurious volumetric stresses are generated by the above boundary conditions.

5.3. CuAlNi shape memory alloy

The computations are carried out for the CuAlNi shape memory alloy undergoing the cubic-to-orthorhombic $\beta_1 \rightarrow \gamma_1'$ transformation that involves six variants of martensite. For this transformation, the crystallographic theory of martensite predicts 96 austenite–twinned martensite interfaces of which four are crystallographically distinct, and the remaining ones are related by the symmetry of the cubic austenite (Bhattacharya, 2003). In the following, the four microstructures will be denoted by M1 to M4 according to Table 1 in (Stupkiewicz et al., 2007), where also the corresponding solutions of the twinning equation and habit plane equation can be found for the variant pair $(I, J) = (1, 3)$.

In all computations the following material parameters are used. The anisotropic elastic constants of single-crystal austenite and martensite, given in Table 1, are taken from the literature (Suezawa and Sumino, 1976; Yasunaga et al., 1983), see also (Sedlák et al., 2005). The interfacial energies γ_{tw} and (isotropic) γ_{am} are adopted as $\gamma_{\mathrm{tw}} = 0.021$ J/m^2 and $\gamma_{\mathrm{am}} = 0.2$ J/m^2 as in (Petryk et al., 2010). Note that those values (especially the latter) are considered to be rough estimates of the corresponding parameters, as more reliable values are currently not available. The interface thickness ℓ is treated as a *numerical* parameter and is selected individually in each case considering the domain size and characteristic dimension of the finite-element mesh. Finally, the mobility parameters, adopted as $L = L_0 = 100$ (Pa s)$^{-1}$, specify the time scale for the microstructure evolution at fixed $\bar{\mathbf{F}}$.

Cubic β_1 phase			Orthorhombic γ_1' phase									
c_{11}	c_{44}	c_{12}	c_{11}	c_{22}	c_{33}	c_{44}	c_{55}	c_{66}	c_{12}	c_{13}	c_{23}	[GPa]
142	96	126	189	141	205	54.9	19.7	62.6	124	45.5	115	

Table 1: Elastic constants of CuAlNi single crystals.

5.4. Twinning in a cylindrical grain

The first numerical example concerns the transformation between two variants of martensite in a circular grain-like domain of diameter $D = 20\,\mathrm{nm}$. The evolution is controlled by the boundary condition given by (58) and (59) with $\bar{\eta}_0 = 0$, and the control parameter $\bar{\eta}$ is prescribed as a function of time t. Initially, at $t = 0$, $\bar{\eta}$ is set to zero. With the increasing time, $\bar{\eta}$ grows linearly up to the value of 1.1, then it decreases to -0.1 and again increases to zero. The problem is computed for two rates of $\bar{\eta}$: higher $0.1\,\mathrm{s}^{-1}$ and lower $0.01\,\mathrm{s}^{-1}$. The finite-element mesh consists of $31\,631$ elements with the average element size $h = 0.1\,\mathrm{nm}$, and the interface thickness parameter is adopted as $\ell = 0.2\,\mathrm{nm}$.

A uniform initial condition $\eta = 0$ is prescribed at $t = 0$ in the whole domain B, and the microstructure formation is triggered by the imperfection (5% perturbation) of the mobility parameter L as indicated in Section 4.2.

Figure 2 shows the snapshots of microstructure evolution, corresponding to $\dot{\bar{\eta}} = 0.01\,\mathrm{s}^{-1}$, taken at time instants denoted by letters 'a' to 'o' and visualized in the current configuration. Orientation of unstressed martensite corresponds to the reference twin plane normal $\mathbf{l}$ in microstructure M1 (Stupkiewicz et al., 2007) inclined horizontally in the figure plane. Current inclination of the traces of sharp twin interfaces, of normal $\hat{\mathbf{l}} = \det(\mathbf{F}_I)\mathbf{F}_I^{-\mathrm{T}}\mathbf{l}$ predicted at zero stress for that microstructure by the crystallographic theory, is marked in the figure by a solid line. It is in excellent agreement with the inclination of the central part of diffuse twin interfaces calculated without the use of the twinning equation (except when defining boundary conditions). Point 'a' corresponds to the control parameter $\bar{\eta} = 0$ with the solution $\eta = 0$ (indicated by red), and point 'o' corresponds to $\bar{\eta} = 1$ with the solution $\eta = 1$ (indicated by blue). The solutions at points 'b' and 'n' do not exhibit any visible microstructure, and the order parameter η is approximately uniform with the value close to 0.2 and 0.9, respectively. At point 'c', the first plate of the product phase is created. Subsequently, the number of plates increases, reaching the maximum at point 'h' that corresponds to $\bar{\eta} = 0.5$, and then the number of plates of the parent phase decreases.

The calculated dependence of $\langle\eta\rangle$, the averaged order parameter, on $\bar{\eta}$ is shown in Fig. 3. References to the snapshots in Fig. 2 are indicated by corresponding letters. Hysteresis loops can be seen, and the hysteresis is bigger for the higher loading rate, which is evidently due to the assumed viscous character of the dissipation.

In order to illustrate the effect of the bound constraints $0 \leq \eta \leq 1$, the results obtained using the model summarized in Box 1 have been compared to those corresponding to the same model but with no bound constraints on η. The latter results are depicted by dashed lines in Fig. 3, and it is clearly seen that the average order parameter $\langle\eta\rangle$ violates the bounds when the control parameter $\bar{\eta}$ exceeds the range $[0, 1]$, which is not the case for our model. Furthermore, when $\bar{\eta}$ exceeds the range $[0, 1]$, a purely elastic stress-strain response is obtained using the model summarized in Box 1, while the corresponding response of the model with no bound constraints is less stiff, as it involves an inelastic contribution associated with non-physical values of the order parameter η. Actually, even for the control parameter $0 \leq \bar{\eta} \leq 1$, there is also a small difference in the solution between the models with and without the bound constraints, which however is not visible on the overall response in Fig. 3.

5.5. Twinning in a cylindrical grain: size effects

In this subsection, the example of the previous subsection is further analysed, and the effect of the diameter D of the circular domain on the microstructure is studied. The boundary condition (58)–(59) with $\bar{\eta}_0 = 0$ and a fixed value of $\bar{\eta} = 0.5$ is now prescribed, and a steady-state solution is computed for different values of D between 6 and $60\,\mathrm{nm}$. For lower values of D, no microstructure is formed, and a solution with uniform η has been obtained. The average element size $h = 0.075\,\mathrm{nm}$ and the interface thickness parameter $\ell = 0.2\,\mathrm{nm}$ are adopted in all computations in Subsection 5.5.

The results corresponding to selected representative values of the diameter D are shown in Fig. 4. As in the previous subsection, the obtained microstructure is essentially a simple laminate. It is evident that the twin spacing depends on the diameter D. Since the spacing is not strictly
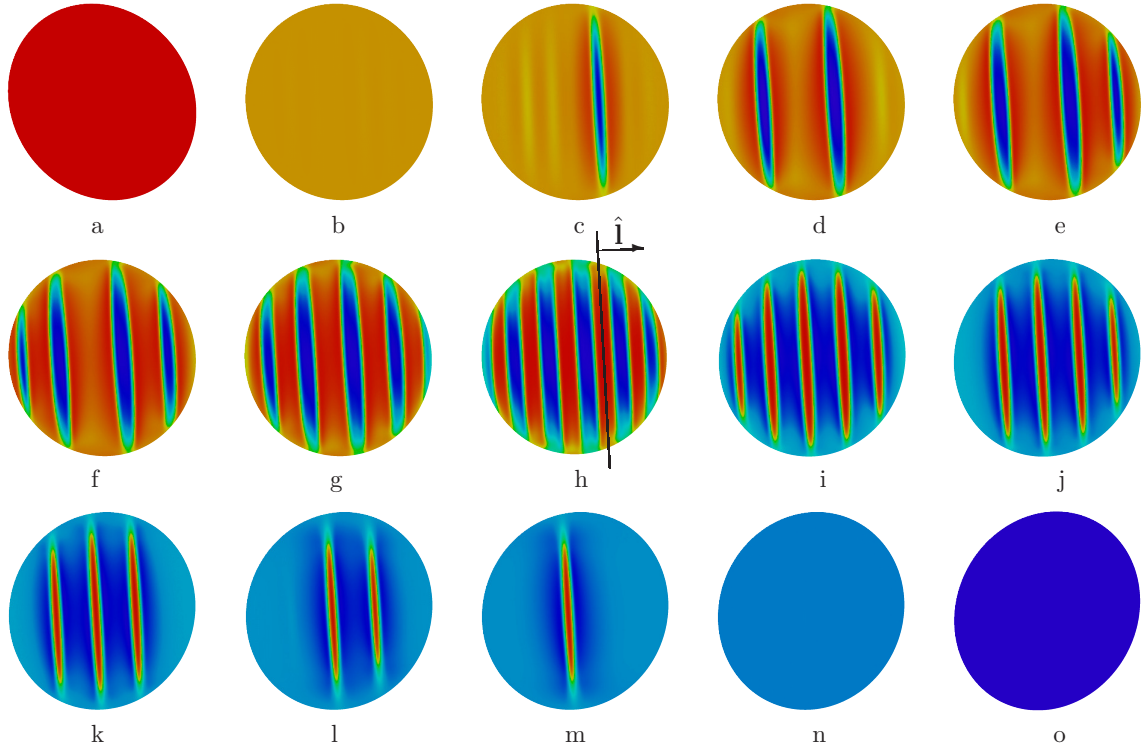
Figure 2: Twinning in a cylindrical grain: snapshots of microstructure evolution in the current configuration ($D = 20\,\text{nm}$, $\ell = 0.2\,\text{nm}$, $\dot{\bar{\eta}} = 0.01\,\text{s}^{-1}$). The color map indicates the value of the order parameter η: red corresponds to $\eta = 0$, blue to $\eta = 1$. Points 'a' to 'o' are also indicated on the hysteresis loop in Fig. 3.
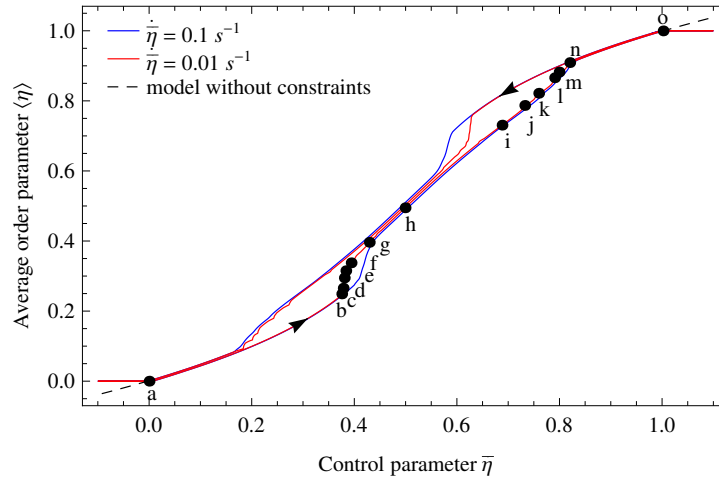

Figure 3: Dependence of the average order parameter $\langle \eta \rangle$ on the control parameter $\bar{\eta}$.

uniform within the grains, the number of diffuse twin interfaces, $\hat{N}_{\text{tw}}$, will be used to quantify their average spacing $\langle \hat{h}_{\text{tw}} \rangle = 2D/\hat{N}_{\text{tw}}$. The graph of the dependence of the number of diffuse interfaces $\hat{N}_{\text{tw}}$ on D is given in Fig. 5 and compared with the theoretical sharp-interface estimate N_{tw} derived in Appendix B.

As shown in Appendix B the twin spacing h_{tw} can be estimated as a geometric mean of the diameter D and a characteristic length $l = 2\gamma_{\text{tw}}/\Gamma_{\text{gb}}^{\text{e}}$, see Eq. (B.10), where γ_{tw} is the interfacial
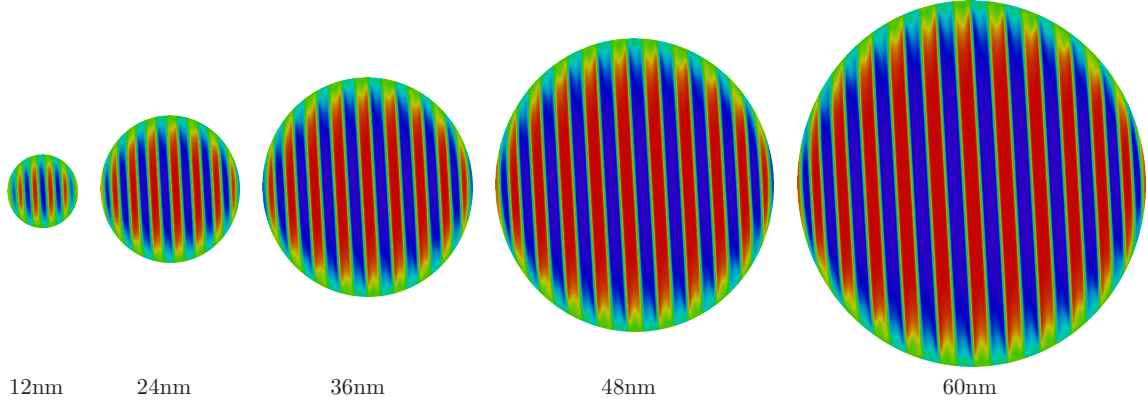
12nm   24nm   36nm   48nm   60nm

Figure 4: Twinning in a cylindrical grain: equilibrium (steady-state) microstructures corresponding to $\bar{\eta} = 0.5$ and to the diameter D equal to $12\,\mathrm{nm}$, $24\,\mathrm{nm}$, $36\,\mathrm{nm}$, $48\,\mathrm{nm}$ and $60\,\mathrm{nm}$ ($\ell = 0.2\,\mathrm{nm}$).
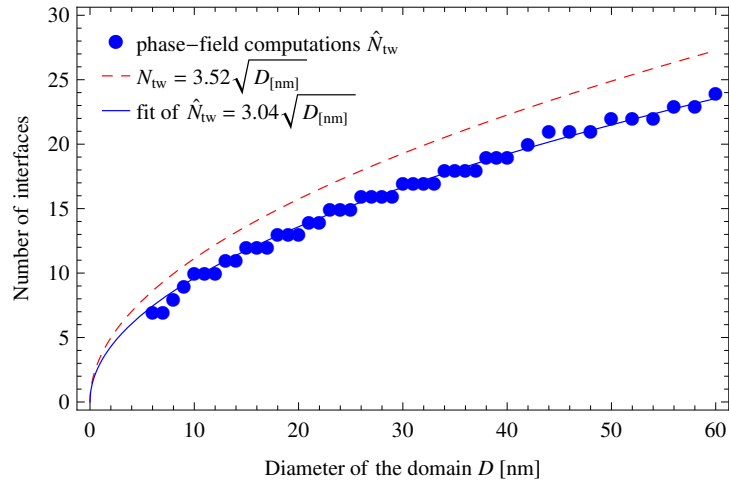

Figure 5: Dependence of the number of twin interfaces on the diameter D of the cylindrical grain. Results of the phase-field computations (blue markers) and their fit by a square-root function (blue line) are compared to the analytic estimate (61) (red dashed line).

energy of twin boundaries, and $\Gamma_{\mathrm{gb}}^{\mathrm{e}}$ is a size-independent energy factor characterizing the elastic micro-strain energy at the grain boundaries, see Eq. (B.9)$_2$. Note that length l determined from the minimization of total interfacial energy has a different meaning than the phase-field parameter ℓ. An estimate for $\Gamma_{\mathrm{gb}}^{\mathrm{e}}$ is given by Eq. (B.8), obtained under the assumption of isotropic linear elasticity. The relevant shear modulus $\mu = 32.7\,\mathrm{GPa}$ and the Poisson's ratio $\nu = 0.3768$ of anisotropic martensite are estimated using the so-called Hill's estimate (Hill, 1952), i.e. by taking the arithmetic mean of the Voigt (upper) and Reuss (lower) bounds of isotropic elastic moduli computed using the actual elastic constants given in Table 1. The remaining parameters $b = |\mathbf{a}| = 0.2538$ and $\beta = 31.9°$ needed to determine $\Gamma_{\mathrm{gb}}^{\mathrm{e}}$ are known from the crystallography. Finally, on substituting $\tilde{\eta} = \bar{\eta} = 0.5$ and $\gamma_{\mathrm{tw}} = 0.021\,\mathrm{J/m^2}$, the characteristic length $l = 0.32\,\mathrm{nm}$ is obtained, and the estimated number of twin interfaces N_{tw} becomes

$$N_{\mathrm{tw}} = 2\frac{D}{h_{\mathrm{tw}}} = 2\sqrt{\frac{D}{l}} \approx 3.52\sqrt{D_{[\mathrm{nm}]}} \tag{61}$$

for $D_{[\mathrm{nm}]}$ expressed in nm. The above prediction is included in Fig. 5. Of course, the non-integer estimate can be rounded off to the nearest integer number.

Since the estimate of the elastic strain energy at the grain boundary used to derive Eq. (61) represents a rough approximation (the laminate is not sufficiently fine with respect to the boundary radius, twin spacing is not uniform, and martensite is highly anisotropic), the estimated number of sharp twin interfaces, Eq. (61), could be expected to deviate quantitatively from the phase-field calculations. Nevertheless, the agreement seen in Fig. 5 is found surprisingly good. Furthermore, the phase-field results follow perfectly the square-root scaling predicted by the theory, see the square-root fit of $\hat{N}_{\mathrm{tw}}$ in Fig. 5. By fitting the phase-field results, the actual characteristic length l is determined as $0.43\,\mathrm{nm}$, as compared to the predicted value of $0.32\,\mathrm{nm}$, so that the quantitative agreement between the solid and dashed lines in Fig. 5 becomes perfect if the energy factor $\Gamma_{\mathrm{gb}}^{\mathrm{e}}$ predicted by formula (B.8) is reduced by $\sim 25\%$.

5.6. Austenite–twinned martensite interface

In this section, the model summarized in Box 2 is applied to study the interface between austenite and twinned martensite. Specifically, we are interested in the interface morphology and the elastic strain energy accumulated in the transition layer for the four representative microstructures (M1, M2, M3, M4), in comparison with the sharp-interface results obtained by Stupkiewicz et al. (2007).

Following the sharp-interface approach with interfacial energy effects in rank-two laminates, developed and described in detail in (Petryk et al., 2006; Maciejewski et al., 2005; Stupkiewicz et al., 2007; Petryk et al., 2010; Stupkiewicz et al., 2012), the problem of finding the equilibrium interface shape is studied here using the phase-field method. For that purpose, a periodic domain B_{per} of the form of a parallelogram in the reference configuration of unstressed austenite is adopted, where the normal to the lateral sides is equal to $\pm\mathbf{l}$ and the normal to the top and bottom sides is equal to $\pm\mathbf{m}$. Periodic conditions specified by Eqs. (60) and (58) are prescribed on the boundary with $\bar{\eta}_0 = 0.5$ and $\bar{\eta} = \hat{\eta}$, where $\hat{\eta}$ is the twin fraction known from the solution of the habit plane equation (55). Periodicity of the displacement $\mathbf{u}$ and order parameters η and η_0 is imposed by using Lagrange multipliers. The microstructure is analysed in an equilibrium temperature, thus the chemical free energy is set to zero, $F_{\mathrm{m}}^0 = F_{\mathrm{a}}^0 = 0$. Distribution of the order parameter η is initially random, and evolution of the system towards a steady state is simulated. The steady-state solution which corresponds to an equilibrium microstructure is then further analysed.

Local incompatibility of transformation strains is necessarily accommodated by elastic strains in a transition layer along the austenite–martensite interface. This energy is interpreted at a higher scale as the interfacial energy. In analogy to the sharp-interface approach referred to above, the density $\gamma_{\mathrm{am}}^{\mathrm{e}}$ of the interfacial energy of elastic micro-strains at austenite–twinned martensite interfaces is defined as the total elastic strain energy referred to the total nominal area A_{R} (taken in the reference configuration) of the macroscopically planar traces of austenite–twinned martensite

interfaces within the simulation cell B_{per}, and the energy factor $\Gamma^{\mathrm{e}}_{\mathrm{am}}$ is determined as follows

$$\gamma^{\mathrm{e}}_{\mathrm{am}} = \frac{1}{A_{\mathrm{R}}} \int_{B_{\mathrm{per}}} F_{\mathrm{B}} \, \mathrm{d}\mathbf{X}, \qquad \Gamma^{\mathrm{e}}_{\mathrm{am}} = \frac{\gamma^{\mathrm{e}}_{\mathrm{am}}}{h_{\mathrm{tw}}}. \qquad (62)$$

We note that the energy factor $\Gamma^{\mathrm{e}}_{\mathrm{am}}$ is not strictly size-independent here because of the variable contribution of the interfacial energy of the direct austenite–martensite interfaces (specifically, the part of F_{Γ} with the density γ_{am}, cf. also Appendix B). The related dependence of $\Gamma^{\mathrm{e}}_{\mathrm{am}}$ on the twin spacing h_{tw} is not studied here.

When defining the interfacial energy in Eq. (62), it is tacitly assumed that the elastic strain energy is concentrated in vicinity of the austenite–twinned martensite interface. This condition is satisfied in principle as a consequence of the adopted definition (58) of the average deformation gradient $\bar{\mathbf{F}}$ that is compatible with the microstructure formed at zero macroscopic stress. However, a relatively small amount of elastic strain energy is present within the twin boundaries, which is typical for Khachaturyan-type interpolation schemes (Durga et al., 2013; Mosler et al., 2014). This is a secondary effect as it has been found to effectively increase γ_{tw} by less than 10%.

For a prescribed height of 600 nm of the computational cell, its width is selected such that it corresponds to one period of the microstructure, i.e. the width is equal to the twin spacing h_{tw}. In turn, the twin spacing h_{tw} is chosen such that it satisfies the square-root scaling law (B.2) discussed in Appendix B. We note that the optimal twin spacing (B.2) depends on the energy factor $\Gamma^{\mathrm{e}}_{\mathrm{am}}$ which (weakly) depends on the twin spacing h_{tw} as mentioned above. Accordingly, several fixed-point iterations are performed in order to get a consistent value of the twin spacing h_{tw}.

The obtained morphologies of the transition layer corresponding to interface thickness parameter $\ell = 1.0$ nm and element size $h = 0.5$ nm are shown in Fig. 6. The larger green areas indicate the austenite, and the green color visible somewhere within the diffuse interfaces separating two variants of martensite is only due to automatic color scaling between red and blue colors used to distingiush the martensite variants, as no austenite is found there. For better visualization, each microstructure is replicated four times, while the actual computational cell is indicated by thin black lines. These lines indicate also the theoretical current inclination of twin boundaries found from eqs. (54) and (55), which in each case are perfectly aligned with the central part of diffuse twin interfaces determined without using these equations in the phase-field model. The corresponding values of the energy factor $\Gamma^{\mathrm{e}}_{\mathrm{am}}$ are also reported in Fig. 6.

The solution, and in particular the energy factor $\Gamma^{\mathrm{e}}_{\mathrm{am}}$, depends on the length-scale parameter ℓ. This effect has been studied numerically, and Fig. 7 shows the dependence of $\Gamma^{\mathrm{e}}_{\mathrm{am}}$ on ℓ. Those computations have been carried out with a fixed ratio $h/\ell = 0.5$, h being the mesh size, so that the mesh is fine enough to properly represent the microstructure formation. For $\ell < 0.5$ nm, the computations become prohibitively expensive due to the increased size of the problem. It can be seen that for ℓ greater than 2 nm the energy factor $\Gamma^{\mathrm{e}}_{\mathrm{am}}$ is practically insensitive to ℓ, however, a significant increase of $\Gamma^{\mathrm{e}}_{\mathrm{am}}$ is obtained for smaller values of ℓ. At the same time, the microstructure is not visibly affected.

In order to estimate the energy factor $\Gamma^{\mathrm{e}}_{\mathrm{am}}$ at the sharp-interface limit $\ell \to 0$, the dependence of $\Gamma^{\mathrm{e}}_{\mathrm{am}}$ on ℓ has been fitted using an exponential function of the form $a_1 + a_2 \exp(-a_3 \ell)$ which apparently provides a very good fit, as shown in Fig. 7. The energy factors $\Gamma^{\mathrm{e}}_{\mathrm{am}}$ predicted by Stupkiewicz et al. (2007) using the sharp-interface approach are also included in Fig. 7, and they agree quite well with the phase-field results extrapolated to $\ell = 0$. The morphologies of the transition layer predicted by the two approaches are similar for microstructure M2, while for microstructures M1, M3 and M4 they are similar at the boundary of one dominating martensite variant only, see Fig. 8 for comparison. This is not unexpected since the atomic-scale interfacial energy on the local austenite-martensite interface, included in the phase-field calculations, temperes interface undulations (cf. Maciejewski et al., 2005; Stupkiewicz et al., 2012) found especially for microstructure M3 in Fig. 8 when that energy was disregarded.

microstructure M1   microstructure M2   microstructure M3   microstructure M4

$5.42\,\mathrm{MJ/m^3}$ $2.82\,\mathrm{MJ/m^3}$ $2.89\,\mathrm{MJ/m^3}$ $5.47\,\mathrm{MJ/m^3}$
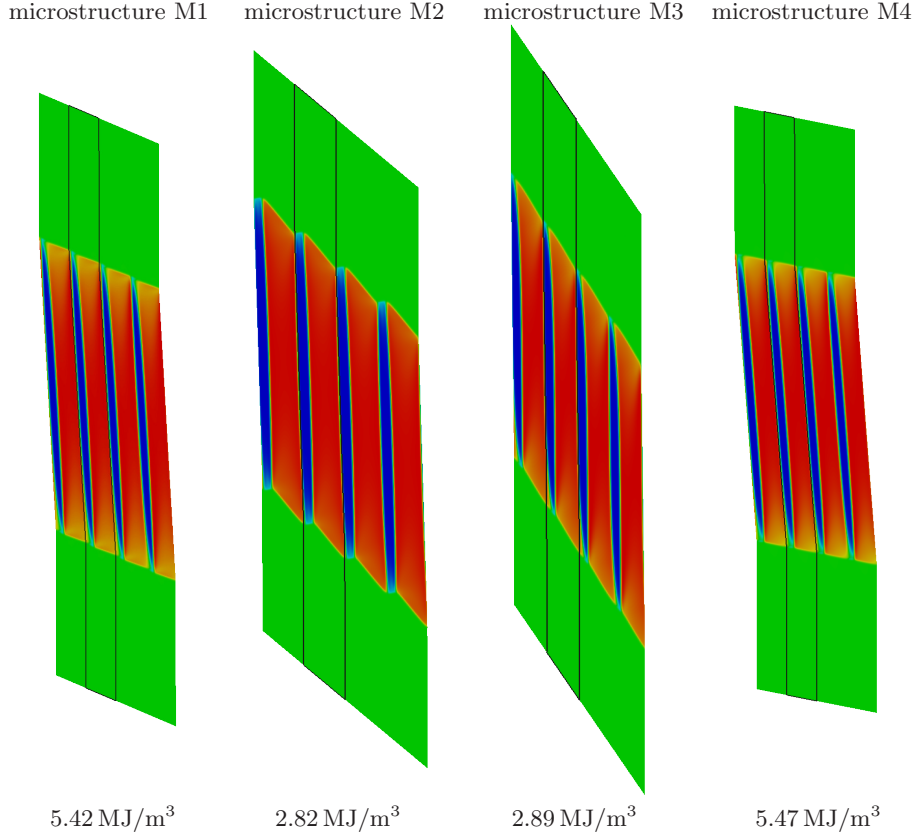
Figure 6: Austenite–twinned martensite interface: steady-state microstructures shown in the current configuration and the corresponding values of the energy factor $\Gamma_{\mathrm{am}}^{\mathrm{e}}$ obtained for $\ell = 1$nm. Variants of martensite are colored by blue and red, and the larger green areas indicate the austenite.

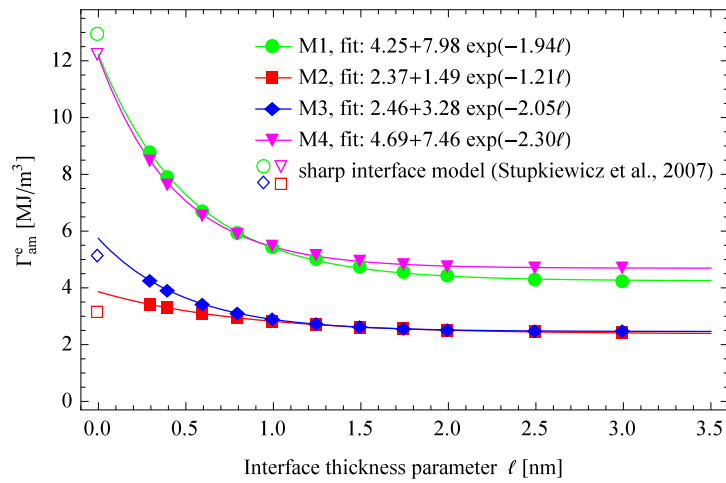Figure 7: Dependence of $\Gamma_{\mathrm{am}}^{\mathrm{e}}$ on ℓ for all microstructures M1 to M4 and the corresponding values obtained by Stupkiewicz et al. (2007) for the sharp-interface model. Results of the phase-field computations (filled markers) and their fits (solid lines) are compared to the predictions of the sharp-interface model (empty markers).
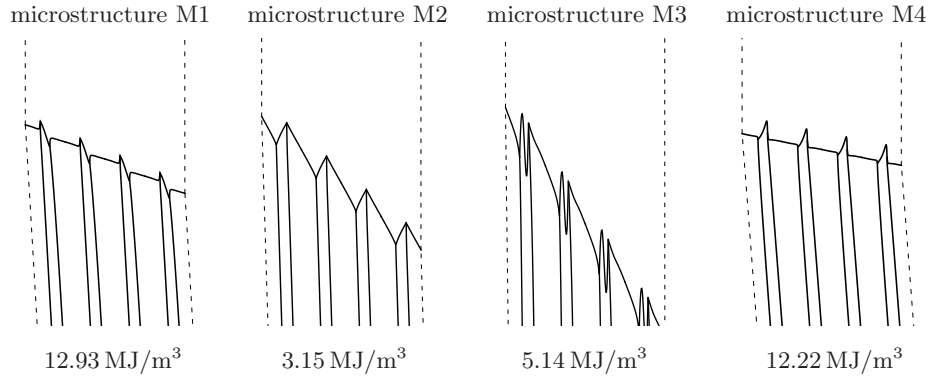
microstructure M1   microstructure M2   microstructure M3   microstructure M4

$12.93\,\mathrm{MJ/m^3}$ $3.15\,\mathrm{MJ/m^3}$ $5.14\,\mathrm{MJ/m^3}$ $12.22\,\mathrm{MJ/m^3}$

Figure 8: Morphology of the austenite–twinned martensite interface obtained using the sharp-interface approach and the corresponding energy factors Γ^e_{am} for interfacial energy $\gamma_{tw} = \gamma_{am} = 0$ at the atomic scale (adopted from Stupkiewicz et al., 2007).

5.7. Austenite–twinned martensite microstructure in a cylindrical grain

In this last problem analysed, the austenite–martensite microstructure is computed in a grain-like circular domain for different values of diameter D in order to study the size effects. As in Section 5.5, the displacement boundary condition (58)–(59) is prescribed, now with $\bar{\eta}_0 = 0.4$ and $\bar{\eta} := \hat{\eta}_{tw}$ found from Eq. (55). Random distribution of order parameters η and η_0 is adopted as the initial condition, and evolution of the system towards a steady-state is simulated. The analysis is now carried out for microstructure M3.

The problem has been computed for several domain sizes D varying between 100 and 700 nm, see Fig. 9. The two variants of martensite are colored by blue and red, and the larger green areas indicate the austenite. It is important to note that there is *no* austenite within the diffuse interfaces between two variants of martensite, and the green color appears there only due to automatic color scaling between blue and red. This is visualized in Fig. 9(e) where in the lower part of the figure the volume fraction of austenite is only displayed. The values of the interface thickness parameter ℓ and average element size h have been selected individually for each domain size D, and these are provided in the caption to Fig. 9.

D [nm]	h_{tw} [nm]	H [nm]	N_{am}	$\hat{N}_{am}$
100	12.4	62.7	3.2	2
200	14.9	90.9	4.4	4
300	16.7	113.1	5.3	4
400	18.0	132.2	6.1	5
500	19.1	149.2	6.7	5
600	20.1	164.8	7.3	6
700	21.0	179.3	7.8	7

Table 2: Estimated twin spacing h_{tw} and austenite–martensite laminate spacing H as a function of diameter D. N_{am} is the corresponding number of austenite–martensite interfaces, while $\hat{N}_{am}$ is the number of interfaces obtained from the phase-field computations.

The obtained microstructure is approximately a rank-two laminate formed by layers of austenite and martensite, the latter being laminates of two twin-related variants of martensite. The morphology of the austenite–twinned martensite interfaces agrees well with that obtained for microstructure M3 in the previous subsection. The inclination of the central parts of the diffuse interfaces is also in a good agreement with theoretical predictions marked, in spite of a relatively small number of austenite layers.

It can be seen in Fig. 9 that the number of layers increases with increasing grain diameter D. Qualitatively, the effect is similar to that observed for the martensite–martensite laminate studied
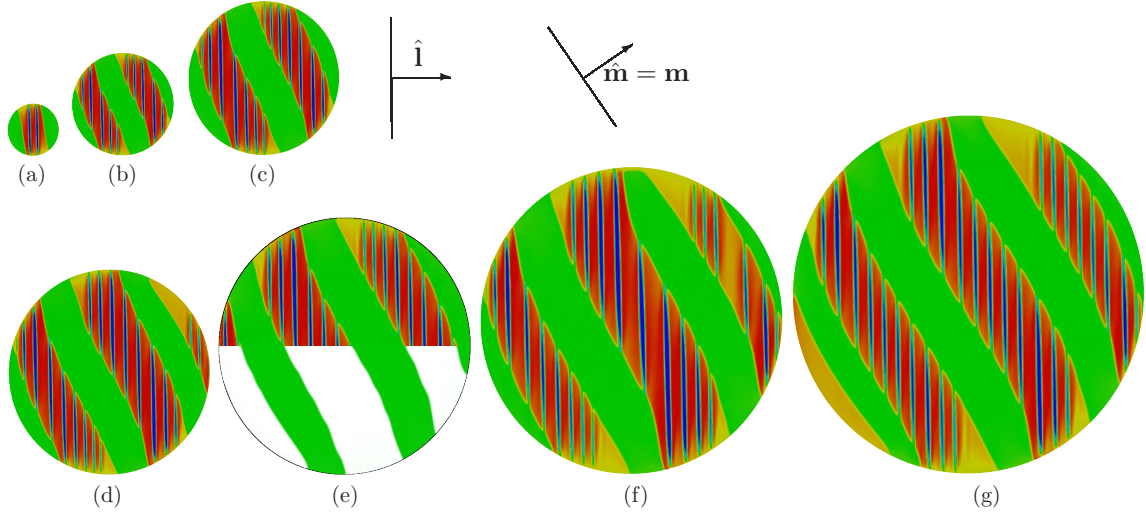
Figure 9: Rank-two austenite–twinned martensite laminates corresponding to microstructure M3: (a) $D = 100\,\text{nm}$ ($\ell = 0.8\,\text{nm}$, $h = 0.4\,\text{nm}$), (b) $D = 200\,\text{nm}$ ($\ell = 0.8\,\text{nm}$, $h = 0.4\,\text{nm}$), (c) $D = 300\,\text{nm}$ ($\ell = 1.0\,\text{nm}$, $h = 0.6\,\text{nm}$), (d) $D = 400\,\text{nm}$ ($\ell = 1.2\,\text{nm}$, $h = 0.7\,\text{nm}$), (e) $D = 500\,\text{nm}$ ($\ell = 1.5\,\text{nm}$, $h = 0.9\,\text{nm}$), (f) $D = 600\,\text{nm}$ ($\ell = 1.8\,\text{nm}$, $h = 1.1\,\text{nm}$), (g) $D = 700\,\text{nm}$ ($\ell = 2.0\,\text{nm}$, $h = 1.2\,\text{nm}$). The larger green areas indicate the austenite, and variants of martensite are colored by blue and red, except the lower part of (e) where the volume fraction of austenite is only displayed.
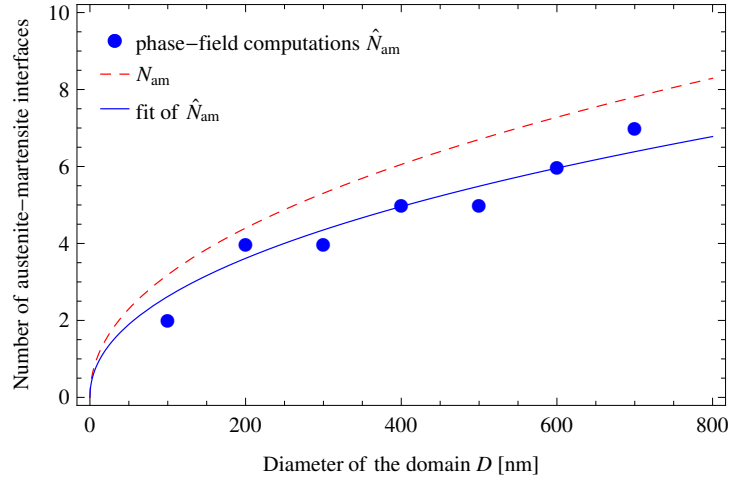

Figure 10: Dependence of the number of austenite–martensite interfaces on the diameter D. Results of the phase-field computations (blue markers) and their fit (blue solid line) are compared to the analytic estimate (red dashed line).

in Section 5.5. A quantitative sharp-interface model for prediction of characteristic dimensions in a periodic rank-two austenite–martensite laminate formed within a circular grain is presented in Appendix B.5. Using this model, the spacing H of the austenite–martensite layers and the twin spacing h_{tw} can be estimated under the assumptions that the interfaces are planar, elasticity is isotropic and the spacings are uniform. Specifically, h_{tw} is found as a solution of the algebraic equation (B.15), and the energetically optimal characteristic dimensions of the microstructure satisfy the square-root scaling rules (B.13)–(B.14).

In order to get equivalent isotropic elastic properties, anisotropic elastic properties of austenite and martensite are approximated using the Hill's estimate, as in Section 5.5, and the following elastic parameters are used in the present calculations: $\mu = 35.3\,\mathrm{GPa}$, $\nu = 0.371$. Parameters $b = |\mathbf{b}| = 0.0932$ and $\beta = 68.4°$ are known from crystallography, so that putting $\tilde{\eta} = 1 - \bar{\eta}_0$ the energy factor $\Gamma_{\mathrm{gb}}^{\mathrm{e}}$ is determined equal to $\Gamma_{\mathrm{gb}}^{\mathrm{e}} = 13.4\,\mathrm{MJ/m^3}$. The remaining parameters needed to estimate the characteristic dimensions are $\gamma_{\mathrm{tw}} = 0.021\,\mathrm{J/m^2}$, $\gamma_{\mathrm{am}} = 0.2\,\mathrm{J/m^2}$, and $\Gamma_{\mathrm{am}}^{\mathrm{e}} = 5.14\,\mathrm{MJ/m^3}$, and $\psi = 1$ is assumed as a first approximation, cf. Appendix B.

The number $\hat{N}_{\mathrm{am}}$ of austenite–martensite interfaces resulting from the phase-field simulations is shown in Fig. 10 and compared with the analytical estimate $N_{\mathrm{am}} = 2D/H$ with the spacing H estimated as described above. The results are also summarized in Table 2. Although the analytical estimate deviates quantitatively from the full phase-field computation, which has been expected in view of the simplifying assumptions made when deriving the estimate, the qualitative prediction is good. It has been found that the phase-field results are well reproduced by the simple sharp-interface model when the energy factor $\Gamma_{\mathrm{gb}}^{\mathrm{e}}$ is reduced by 31% (blue solid line in Fig. 10).

6. Conclusion

Size-dependent microstructures involving twinned martensite and austenite have been examined by using two different approaches: the phase-field method at finite strain and the sharp-interface treatment with interfacial energy effects. The quantitative comparison of the respective results has been presented here for the first time, by the examples calculated for the cubic-to-orthorhombic martensitic transformation in a CuAlNi shape memory alloy. The finite-strain phase-field model used for that purpose has been developed as a novel extension of related earlier models, and the sharp-interface energy approach has followed strictly the earlier works of our group. The agreement between the results calculated by using the finite-element phase-field model and the sharp-interface approach with the assumption of perfect laminates has been found satisfactory, sometimes even surprisingly good in view of the simplifying assumptions involved in the latter approach.

The proposed finite-strain phase-field model of martensitic transformation is based on transparent assumptions regarding the phase mixture properties within diffuse interfaces. The novelty here lies in the linear mixing of logarithmic transformation strains, which ensures volume preservation during twinning and avoids thus a spurious volumetric strain energy. The physically different nature of phase interfaces and twin boundaries is reflected by introducing two order-parameters in a hierarchical manner, one defining the total reference volume fraction of martensite and the second defining the relative content of two variants of martensite. This has lead to clear separation of austenite–martensite and martensite–martensite interfaces in the model and numerical results. In the general variational scheme of phase-field modelling, a nontrivial transition from the variational rate formulation to the incremental one has been demonstrated. It has also been proposed to enforce the physical constraints on volume fractions strictly, and not only in a typical approximate way. For this purpose, the augmented Lagrangian method has been used and shown to work effectively by the examples of more than one million degrees of freedom.

Appendix A. Explicit form of phase-field equations for austenite and two variants of martensite

In this appendix, the basic field equations satisfied by a solution to the variational rate-problem (40) are provided in an explicit form. Specifically, the equilibrium equation and the evolution

26

equations for order parameters η_0 and η read:

$$\mathbf{0} = \frac{\delta \mathcal{F}}{\delta \mathbf{u}} = -\nabla \cdot \mathbf{S}^{\mathrm{T}}, \tag{A.1}$$

$$\dot{\eta}_0 = -L_0 \frac{\delta \mathcal{F}}{\delta \eta_0} \qquad \text{for } 0 < \eta_0 < 1, \tag{A.2}$$

$$(1 - \eta_0)\dot{\eta} = -L \frac{\delta \mathcal{F}}{\delta \eta} \qquad \text{for } 0 < \eta < 1, \tag{A.3}$$

while the case when η_0 or η is equal to 0 or 1 is analogous to that in Eq. (4). The explicit form of the variational derivatives in Eqs. (A.2) and (A.3) is

$$\frac{\delta \mathcal{F}}{\delta \eta_0} = -3\ell\gamma_{\mathrm{am}}\nabla \cdot \nabla\eta_0 + \frac{12\gamma_{\mathrm{am}}}{\ell}\eta_0(1 - \eta_0)(1 - 2\eta_0) - \frac{6\gamma_{\mathrm{tw}}}{\ell}\eta^2(1 - \eta)^2$$
$$+ \left(\mathbf{U}_{\mathrm{t}}^{-1}\mathbf{F}^{\mathrm{T}}\mathbf{S} - F_{\mathrm{B}}\mathbf{U}_{\mathrm{t}}^{-1}\right) \cdot \left(\frac{\partial \exp(\log \mathbf{U}_{\mathrm{t}})}{\partial \log \mathbf{U}_{\mathrm{t}}}\left(\eta \log \mathbf{U}_I + (1 - \eta)\log \mathbf{U}_J\right)\right)$$
$$+ \frac{1}{2}(\det \mathbf{U}_{\mathrm{t}})\mathbf{E}_{\mathrm{e}} \cdot (\mathbf{L}_{\mathrm{a}} - \eta\mathbf{L}_I - (1 - \eta)\mathbf{L}_J)\,\mathbf{E}_{\mathrm{e}}, \quad \text{(A.4)}$$

$$\frac{\delta \mathcal{F}}{\delta \eta} = -3\ell\gamma_{\mathrm{tw}}\nabla \cdot \nabla\eta + (1 - \eta_0)\frac{12\gamma_{\mathrm{tw}}}{\ell}\eta(1 - \eta)(1 - 2\eta)$$
$$+ (1 - \eta_0)\left(\mathbf{U}_{\mathrm{t}}^{-1}\mathbf{F}^{\mathrm{T}}\mathbf{S} - F_{\mathrm{B}}\mathbf{U}_{\mathrm{t}}^{-1}\right) \cdot \left(\frac{\partial \exp(\log \mathbf{U}_{\mathrm{t}})}{\partial \log \mathbf{U}_{\mathrm{t}}}\left(\log \mathbf{U}_J - \log \mathbf{U}_I\right)\right)$$
$$+ \frac{1}{2}(1 - \eta_0)(\det \mathbf{U}_{\mathrm{t}})\mathbf{E}_{\mathrm{e}} \cdot (\mathbf{L}_I - \mathbf{L}_J)\,\mathbf{E}_{\mathrm{e}}. \quad \text{(A.5)}$$

The derivative of tensor exponential results from the differentiation of the logarithmic mixing rule (34). If the tensor logarithm and exponential functions are approximated to the first order, namely $\log \mathbf{X} \approx \mathbf{X} - \mathbf{I}$, $\exp \mathbf{X} \approx \mathbf{I} + \mathbf{X}$, then this derivative is approximated by the fourth-order identity tensor over the space of symmetric tensors, and the above variational derivatives simplify to the respective forms that correspond to linear mixing of transformation stretches, $\mathbf{U}_{\mathrm{t}}^* = \eta_0\mathbf{I} + (1 - \eta_0)(\eta\mathbf{U}_I + (1 - \eta)\mathbf{U}_J)$.

Appendix B. Characteristic dimensions in laminated microstructures

In the appendix, simple estimates are provided for characteristic dimensions of sufficiently fine laminate microstructures with sharp interfaces under the simplifying assumption of small deformations. The estimates are obtained by minimization of the total interfacial energy that comprises size-dependent contributions corresponding to individual scales of the microstructures under consideration.

Appendix B.1. Twin spacing in a twinned martensite plate

Consider a twinned martensite plate of thickness M and twin spacing h_{tw} formed within an austenite matrix. Two types of interfacial energy are considered, namely the atomic-scale energy and the elastic micro-strain energy. The density of the atomic-scale energy of twin boundaries is denoted by γ_{tw} and that of the austenite–martensite interfaces by γ_{am}. The elastic micro-strain energy is associated with the austenite–twinned martensite interfaces and it results from local incompatibility between austenite and martensite variants which is accommodated by elastic strains. The density $\gamma_{\mathrm{am}}^{\mathrm{e}}$ of that energy (per unit area of the macroscopic austenite–martensite interface) is proportional to the twin spacing h_{tw}, so that $\gamma_{\mathrm{am}}^{\mathrm{e}} = \Gamma_{\mathrm{am}}^{\mathrm{e}}h_{\mathrm{tw}}$, where $\Gamma_{\mathrm{am}}^{\mathrm{e}}$ is a size-independent energy factor, see (Khachaturyan, 1983; Maciejewski et al., 2005).

The total interfacial energy Φ_i (per unit volume of the plate) comprising the energy of twin boundaries Φ_{tw} and the energy of austenite–martensite interfaces Φ_{am} is equal to

$$\Phi_i = \Phi_{tw} + \Phi_{am}, \quad \Phi_{tw} = \frac{2\gamma_{tw}}{h_{tw}}, \quad \Phi_{am} = \frac{2(\Gamma^e_{am} h_{tw} + \psi\gamma_{am})}{M}, \tag{B.1}$$

where the density of twin boundaries per unit plate volume is $2/h_{tw}$, density of austenite–martensite interfaces is $2/M$, and $\psi \approx 1$ is the ratio of the total area of the austenite–martensite interfaces at the micro-scale to the macroscopic area. If the total interfacial energy Φ_i is minimized with respect to h_{tw}, one gets a square-root dependence of the twin spacing h_{tw} on plate thickness M (Khachaturyan, 1983),

$$h_{tw} = \sqrt{lM}, \quad l = \frac{\gamma_{tw}}{\Gamma^e_{am}}, \tag{B.2}$$

where l is a characteristic dimension defined by the interfacial energy parameters γ_{tw} and Γ^e_{am}.

Appendix B.2. Boundary layer at a planar microstructured interface

A general approximate formula for the elastic micro-strain energy of a planar interface between an elastic half-space and a laminated half-space has been constructed and calibrated by Petryk et al. (2010). The laminate of spacing H and volume fraction $\tilde{\eta}$ of one family of layers is characterized by a piecewise-constant eigenstrain such that the difference of eigenstrains is a shear strain of the form $\Delta\varepsilon^t = \frac{1}{2}(\mathbf{m} \otimes \mathbf{b} + \mathbf{b} \otimes \mathbf{m})$, where $\mathbf{m}$ is the normal to laminate interfaces, $\mathbf{b}$ satisfies $\mathbf{b} \cdot \mathbf{m} = 0$, and $b = |\mathbf{b}|$ is the shear magnitude. Assuming that the elastic properties are isotropic and homogeneous, with μ and ν denoting the shear modulus and Poisson's ratio, respectively, the interfacial energy γ^e of elastic micro-strains is given by

$$\gamma^e = \mu b^2 \Gamma^e_* H, \tag{B.3}$$

where the dimensionless energy factor Γ^e_* is well approximated by the following formula

$$\Gamma^e_* = a \cos\alpha \frac{1 - \nu \sin^2\beta}{1 - \nu} \left(\tilde{\eta}^2 \left(1 - \sin\frac{\pi\tilde{\eta}}{2} \right)^2 + (1 - \tilde{\eta})^2 \left(1 - \cos\frac{\pi\tilde{\eta}}{2} \right)^2 \right), \tag{B.4}$$

and where $a = 0.197$ is a single universal coefficient that has been determined by fitting the finite-element results. The energy factor Γ^e_* depends also on angles α and β that characterize, respectively, the inclination of the laminate with respect to the interface and the out-of-plane orientation of the shear vector $\mathbf{b}$, see (Petryk et al., 2010).

In the case of an interface between a laminated half-space and a rigid half-space, the corresponding interfacial energy $\gamma^{e,r}$ can be approximated as

$$\gamma^{e,r} \approx 2\mu b^2 \Gamma^e_* H. \tag{B.5}$$

The factor of two in the above formula is found by appealing to the superposition principle in case of constrained both normal and tangential displacements. Clearly, this simple reasoning is approximate because in the original problem the tangential strains are not constrained. Accordingly, the actual factor is somewhat higher than two (typically by 5 to 30% depending on the geometrical parameters), as confirmed by finite-element computations.

Appendix B.3. Elastic micro-strain energy for a laminated cylindrical grain

In this section, the energy of elastic micro-strains is estimated for a laminated cylindrical grain of diameter D embedded in a rigid matrix. Following Stupkiewicz and Petryk (2010), the total energy of elastic micro-strains at the grain boundary of a laminated cylindrical grain embedded in a rigid matrix is obtained by integrating $\gamma^{e,r}$ over the cylindrical boundary ∂B,

$$\Phi_{gb}|B| = \int_{\partial B} \gamma^{e,r}\, dS = 2\int_{-\pi/2}^{\pi/2} \gamma^{e,r} \frac{D\, d\alpha}{2}, \quad |B| = \frac{\pi D^2}{4}, \tag{B.6}$$

where Φ_{gb} is the density per unit volume of the grain under the assumption that the laminate spacing $H \ll D$. The integration gives

$$\Phi_{\mathrm{gb}} = \Gamma_{\mathrm{gb}}^{\mathrm{e}} \frac{H}{D}, \tag{B.7}$$

where

$$\Gamma_{\mathrm{gb}}^{\mathrm{e}} = \frac{16a\mu b^2}{\pi} \frac{1 - \nu \sin^2 \beta}{1 - \nu} \left(\tilde{\eta}^2 \left(1 - \sin \frac{\pi \tilde{\eta}}{2} \right)^2 + (1 - \tilde{\eta})^2 \left(1 - \cos \frac{\pi \tilde{\eta}}{2} \right)^2 \right). \tag{B.8}$$

Appendix B.4. Simple laminate of twinned martensite within a cylindrical grain

Referring to the phase-field computations reported in Sections 5.4 and 5.5, we consider a sufficiently fine, simple laminate of twinned martensite within a cylindrical grain embedded in a rigid matrix. The total interfacial energy Φ_{i} (density per unit volume) consists of the energy Φ_{tw} of twin boundaries and the elastic micro-strain energy at the grain boundary Φ_{gb}, cf. Eq. (B.7), where $H = h_{\mathrm{tw}}$ is the twin spacing, thus

$$\Phi_{\mathrm{i}} = \Phi_{\mathrm{tw}} + \Phi_{\mathrm{gb}}, \qquad \Phi_{\mathrm{tw}} = \frac{2\gamma_{\mathrm{tw}}}{h_{\mathrm{tw}}}, \qquad \Phi_{\mathrm{gb}} = \Gamma_{\mathrm{gb}}^{\mathrm{e}} \frac{h_{\mathrm{tw}}}{D}. \tag{B.9}$$

Minimization of Φ_{i} with respect to h_{tw} gives

$$h_{\mathrm{tw}} = \sqrt{lD}, \qquad l = \frac{2\gamma_{\mathrm{tw}}}{\Gamma_{\mathrm{gb}}^{\mathrm{e}}}, \tag{B.10}$$

so that a square-root dependence is obtained similar to that for a twinned plate, see Eq. (B.2).

Appendix B.5. Rank-two laminate within a cylindrical grain of diameter D

Consider now an austenite–martensite laminate in a cylindrical grain of diameter D in which the martensite layers are internally twinned. The microstructure is thus a rank-two laminate, assumed to be sufficiently fine at each level. The spacing of martensite plates is H, the spacing of twins within the twinned martensite plates is h_{tw}, and the volume fraction of martensite is denoted by $\tilde{\eta}$ so that the martensite plate thickness is $M = \tilde{\eta}H$.

Following Petryk et al. (2010) and Stupkiewicz and Petryk (2010), the total interfacial energy density Φ_{i} (per unit volume of the grain) comprises the energy of twin interfaces Φ_{tw}, the energy of austenite–martensite interfaces Φ_{am} consisting of the atomic-scale and elastic micro-strain energy, and the energy Φ_{gb} of elastic micro-strains at the grain boundary, computed according to Eq. (B.7),

$$\Phi_{\mathrm{i}} = \Phi_{\mathrm{tw}} + \Phi_{\mathrm{am}} + \Phi_{\mathrm{gb}}, \quad \Phi_{\mathrm{tw}} = \frac{2\tilde{\eta}\gamma_{\mathrm{tw}}}{h_{\mathrm{tw}}}, \quad \Phi_{\mathrm{am}} = \frac{2(\Gamma_{\mathrm{am}}^{\mathrm{e}} h_{\mathrm{tw}} + \psi \gamma_{\mathrm{am}})}{H}, \quad \Phi_{\mathrm{gb}} = \Gamma_{\mathrm{gb}}^{\mathrm{e}} \frac{H}{D}. \tag{B.11}$$

The energy densities Φ_{tw} and Φ_{am} are here referred to the unit volume of the grain, while in Eq. (B.1) the densities Φ_{tw} and Φ_{am} are referred to the unit volume of martensite, hence the corresponding formulae differ by the factor of $\tilde{\eta}$.

The necessary conditions for the minimum of Φ_{i} with respect to h_{tw} and H are the following

$$\frac{\partial \Phi_{\mathrm{i}}}{\partial h_{\mathrm{tw}}} = 0, \qquad \frac{\partial \Phi_{\mathrm{i}}}{\partial H} = 0. \tag{B.12}$$

Those conditions can be expressed in the form of two square-root dependencies,

$$h_{\mathrm{tw}} = \sqrt{lM}, \qquad l = \frac{\gamma_{\mathrm{tw}}}{\Gamma_{\mathrm{am}}^{\mathrm{e}}}, \qquad M = \tilde{\eta}H, \tag{B.13}$$

$$M = \sqrt{l_{\mathrm{s}}D}, \qquad l_{\mathrm{s}} = \frac{2\tilde{\eta}^2(\Gamma_{\mathrm{am}}^{\mathrm{e}} h_{\mathrm{tw}} + \psi \gamma_{\mathrm{am}})}{\Gamma_{\mathrm{gb}}^{\mathrm{e}}}. \tag{B.14}$$

The expression for the twin spacing h_{tw} is identical to that obtained for the twinned plate, Eq. (B.1). However, the characteristic dimension l_{s}, which is involved in the formula for the plate thickness M, depends on h_{tw}, hence the following fourth-order algebraic equation for h_{tw} must be solved numerically,

$$\frac{\Gamma_{\mathrm{gb}}^{\mathrm{e}}}{D}\left(\frac{\Gamma_{\mathrm{am}}^{\mathrm{e}}}{\tilde{\eta}\gamma_{\mathrm{tw}}}\right)^2 h_{\mathrm{tw}}^4 - 2\Gamma_{\mathrm{am}}^{\mathrm{e}}h_{\mathrm{tw}} - 2\psi\gamma_{\mathrm{am}} = 0. \tag{B.15}$$

It can be easily shown that the Hessian of Φ_{i} with respect to (H, h_{tw}) is positive definite and thus the minimum is attained.

References

Ahluvalia, R., Lookman, T., Saxena, A., Albers, R. C., 2004. Landau theory for shape memory polycrystals. Acta Mater. 52, 209–218.

Alart, P., Curnier, A., 1991. A mixed formulation for frictional contact problems prone to Newton like solution methods. Comp. Meth. Appl. Mech. Engng. 92, 353–375.

Artemev, A., Wang, Y., Khachaturyan, A. G., 2000. Three-dimensional phase field model and simulation of martensitic transformation in multilayer systems under applied stresses. Acta Mater. 48, 2503–2518.

Aubry, S., Fago, M., Ortiz, M., 2003. A constrained sequential-lamination algorithm for the simulation of sub-grid microstructure in martensitic materials. Comp. Meth. Appl. Mech. Engng. 192, 2823–2843.

Ball, J. M., James, R. D., 1987. Fine phase mixtures as minimizers of energy. Arch. Ration. Mech. Anal. 100, 13–50.

Bertsekas, D. P., 1996. Constrained Optimization and Lagrange Multiplier Methods, 2nd Edition. Athena Scientific, Belmont, MA.

Bhattacharya, K., 2003. Microstructure of martensite: why it forms and how it gives rise to the shape-memory effect. Oxford University Press, Oxford.

Chen, L. Q., 2002. Phase-field models for microstructure evolution. Annu. Rev. Mater. Res. 32, 113–140.

Clayton, J. D., Knap, J., 2011. A phase field model of deformation twinning: Nonlinear theory and numerical simulations. Physica D 240, 841–858.

Durga, A., Wollants, P., Moelans, N., 2013. Evaluation of interfacial excess contributions in different phase-field models for elastically inhomogeneous systems. Modelling Simul. Mater. Sci. Eng. 21, 055018.

Fischer, F. D., Svoboda, J., Petryk, H., 2014. Thermodynamic extremal principles for irreversible processes in materials science. Acta Mater. 67, 1–20.

Hildebrand, F. E., Miehe, C., 2012. A phase field model for the formation and evolution of martensitic laminate microstructure at finite strains. Phil. Mag. 92, 4250–4290.

Hill, R., 1952. The elastic behaviour of a crystalline aggregate. Proc. Phys. Soc. Lond. A 65, 349–354.

Jin, Y. M., Artemev, A., Khachaturyan, A. G., 2001. Three-dimensional phase field model of low-symmetry martensitic transformation in polycrystal: simulation of ζ_2' martensite in AuCd alloys. Acta Mater. 49, 2309–2320.

Khachaturyan, A. G., 1983. Theory of Structural Transformations in Solids. John Wiley and Sons, New York.

Korelc, J., 2002. Multi-language and multi-environment generation of nonlinear finite element codes. Engineering with Computers 18, 312–327.

Korelc, J., 2009. Automation of primal and sensitivity analysis of transient coupled problems. Comp. Mech. 44, 631–649.

Korelc, J., Stupkiewicz, S., 2014. Closed-form matrix exponential and its application in finite-strain plasticity. Int. J. Num. Meth. Engng. 98, 960–987.

Kružík, M., Mielke, A., Roubíček, T., 2005. Modelling of microstructure and its evolution in shape-memory-alloy single-crystals, in particular in CuAlNi. Meccanica 40, 389–418.

Lei, C. H., Li, L. J., Shu, Y. C., Li, J. Y., 2010. Austenite–martensite interface in shape memory alloys. Appl. Phys. Lett. 96, 141910.

Levin, V. A., Levitas, V. I., Zingerman, K. M., Freiman, E. I., 2013. Phase-field simulation of stress-induced martensitic phase transformations at large strains. Int. J. Sol. Struct. 50, 2914–2928.

Levitas, V. I., 2014. Phase field approach to martensitic phase transformations with large strains and interface stresses. J. Mech. Phys. Solids 70, 154–189.

Levitas, V. I., Levin, V. A., Zingerman, K. M., Freiman, E. I., 2009. Displacive phase transitions at large strains: phase-field theory and simulations. Phys. Rev. Lett. 103, 025702.

Levitas, V. I., Preston, D. L., 2002. Three-dimensional Landau theory for multivariant stress-induced martensitic phase transformations. I. Austenite↔martensite. Phys. Rev. B 66, 134206.

Maciejewski, G., Stupkiewicz, S., Petryk, H., 2005. Elastic micro-strain energy at the austenite–twinned martensite interface. Arch. Mech. 57, 277–297.

Mamivand, M., Zaeem, M. A., El Kadiri, H., 2013. A review on phase field modeling of martensitic phase transformation. Comput. Mater. Sci. 77, 304–311.

Moelans, N., Blanpain, B., Wollants, P., 2008. An introduction to phase-field modeling of microstructure evolution. Calphad 32, 268–294.

Mosler, J., Shchyglo, O., Hojjat, H. M., 2014. A novel homogenization method for phase field approaches based on partial rank-one relaxation. J. Mech. Phys. Solids 68, 251–266.

Otsuka, K., Wayman, C. M. (Eds.), 1998. Shape Memory Materials. Cambridge University Press.

Penrose, O., Fife, P. C., 1990. Thermodynamically consistent models of phase-field type for the kinetic of phase transitions. Physica D 43, 44–62.

Petryk, H., Stupkiewicz, S., 2012. Instability of equilibrium of evolving laminates in pseudo-elastic solids. Int. J. Non-Linear Mech. 47, 317–330.

Petryk, H., Stupkiewicz, S., Maciejewski, G., 2006. Modelling of austenite/martensite laminates with interfacial energy effect. In: Sun, Q. P., Tong, P. (Eds.), IUTAM Symposium on Size Effects on Material and Structural Behavior at Micron- and Nano-scales, Hong-Kong 2004. Vol. 142 of Solid Mechanics and its Applications. Springer, pp. 151–162.

Petryk, H., Stupkiewicz, S., Maciejewski, G., 2010. Interfacial energy and dissipation in martensitic phase transformations. Part II: Size effects in pseudoelasticity. J. Mech. Phys. Solids 58, 373–389.

Roytburd, A. L., 1998. Thermodynamics of polydomain heterostructures. II. Effect of microstresses. J. Appl. Phys. 83, 239–245.

Sedlák, P., Seiner, H., Landa, M., Novák, V. Šittner, P., Manosa, L., 2005. Elastic constants of bcc austenite and 2H orthorhombic martensite in CuAlNi shape memory alloy. Acta Mater. 53, 3643–3661.

Shu, Y. C., Yen, J. H., 2008. Multivariant model of martensitic microstructure in thin films. Acta Mater. 56, 3969–3981.

Steinbach, I., 2009. Phase-field models in materials science. Modelling Simul. Mater. Sci. Eng. 17, 073001.

Stupkiewicz, S., Maciejewski, G., Petryk, H., 2007. Low-energy morphology of the interface layer between austenite and twinned martensite. Acta Mater. 55, 6292–6306.

Stupkiewicz, S., Maciejewski, G., Petryk, H., 2012. Elastic micro-strain energy of austenite-martensite interface in NiTi. Modelling Simul. Mater. Sci. Eng. 20, 035001.

Stupkiewicz, S., Petryk, H., 2010. Grain-size effect in micromechanical modelling of hysteresis in shape memory alloys. ZAMM 90, 783–795.

Stupkiewicz, S., Petryk, H., 2013. A robust model of pseudoelasticity in shape memory alloys. Int. J. Num. Meth. Engng. 93, 747–769.

Suezawa, M., Sumino, K., 1976. Behaviour of elastic constants in Cu-Al-Ni alloy in the close vicinity of M_s-point. Scripta Metall. 10, 789–792.

Wang, Y., Khachaturyan, A. G., 1997. Three-dimensional field model and computer modeling of martensitic transformations. Acta Mater. 45, 759–773.

Wang, Y., Li, J., 2010. Phase field modeling of defects and deformation. Acta Mater. 58, 1212–1235.

Wechsler, M. S., Lieberman, D. S., Read, T. A., 1953. On the theory of the formation of martensite. Trans. AIME J. Metals 197, 1503–1515.

Yasunaga, M., Funatsu, Y., Kojima, S., Otsuka, K., Suzuki, T., 1983. Measurement of elastic constants. Scripta Metall. 17, 1091–1094.